



# Multi-interfacial dendritic engineering facilitating congruous intrinsic activity of oxide-carbide/MOF nanostructured multimodal electrocatalyst for hydrogen and oxygen electrocatalysis

Dasu Ram Paudel<sup>a,b</sup>, Uday Narayan Pan<sup>a</sup>, Ram Babu Ghising<sup>a</sup>, Mani Ram Kandel<sup>a</sup>, Sampath Prabhakaran<sup>a</sup>, Do Hwan Kim<sup>c</sup>, Nam Hoon Kim<sup>a,\*</sup>, Joong Hee Lee<sup>a,d,\*\*</sup>

<sup>a</sup> Department of Nano Convergence Engineering (BK21 Four), Jeonbuk National University, Jeonju, Jeonbuk 54896, Republic of Korea

<sup>b</sup> Department of Chemistry, Tri-Chandra Multiple Campus, Tribhuvan University, Kathmandu 44613, Nepal

<sup>c</sup> Division of Science Education, Graduate School of Department of Energy Storage/Conversion Engineering, Jeonbuk National University Jeonju, Jeonju, Jeonbuk 54896 Republic of Korea

<sup>d</sup> Carbon Composite Research Centre, Department of Polymer-Nano Science and Technology, Jeonbuk National University, Jeonju, Jeonbuk 54896, Republic of Korea

## ARTICLE INFO

### Keywords:

Dendritic nanostructure  
Multiple interfaces  
Water splitting  
Multifunctional electrocatalyst  
Zinc-air battery

## ABSTRACT

Multiple interfaces and phases between the electrode and electrolyte play a key role in prompting the overall electrocatalysis, due to the high chances of the formation and cleavage of chemical bonds. Here, we employed the most common tactic of coupling functional components into a hybrid heterostructure with improved synergistic effects between organic and inorganics. The functional metal nodes-organic bridge ligands integrated on polyvalent tungsten oxide-carbide interfaces with highly-porous nano-dendritic architectonic is developed. The FeCu-BTC/WO<sub>3</sub>-WC showed excellent electrochemical half-cell (HER/OER/ORR), and Full-cell (aqueous ZAB and water electrolysis) performances with  $E_{1/2, ORR} = 0.81$  V,  $\eta_{10, OER} = 249$  mV,  $\eta_{10, HER} = 99$  mV,  $E_{10, water splitting} = 1.531$  V, and  $PD_{ZAB} = 135.2$  mW cm<sup>-2</sup> with profound durability. Hence, the multi-interfacial dendritic FeCu-BTC/WO<sub>3</sub>-WC ternary nanocomposite offers the prospect of a good harbinger for aggressive reform of energy technologies towards the zero-emission energy goal.

## 1. Introduction

The environmental calamity due to the relentless use of fossil fuels for over a century has prompted the edicts for carbon neutrality and net zero emissions achievements [1]. The increasing endeavors that are devoted to alternative environment friendly energy sources as a complementary source to fossil fuels include carbon-free green hydrogen (H<sub>2</sub> fuel), and clean energy devices, like fuel cells and metal-air batteries [2, 3]. The generation of H<sub>2</sub> gas via the typical water electrolysis is an environmentally benign, efficient, and low-cost approach that comprises hydrogen evolution reaction (HER) at the cathodic half-cell, and the corresponding oxygen evolution reaction (OER) at the anodic half-cell [3,4]. The electrochemical redox-coupled OER and oxygen reduction reaction (ORR) is the core reaction at the air electrodes in regenerative fuel cells and metal-air batteries [5,6]. These promising technologies are still obstructed by the thermodynamically arduous reactions (HER,

OER, and ORR) with slow kinetics, and high overpotential [1,7]. Currently, precious metals (e.g., Pt, Pd, Ru, and Ir) ensure the expected performance towards HER, OER, and ORR, but the viability in commercial applications is still limited, owing to their natural scarcity, surging cost, and poor stability [8,9]. Thus, a bountiful, stable, and noble metal-free active multifunctional electrocatalyst that can enhance the electron-to-hydrogen conversion efficiency by lowering the energy of activation is earnest for incipient renewable energy technologies, such as fuel cells, metal-air batteries, and electrolyzer [10].

Specifically, transition metal oxides (TMOs) and transition metal carbides (TMCs) integrated with multi-interfacial heterostructure are appealing materials for electrocatalytic activity due to their distinctive structural features, stable electronic properties, and mutual synergism [11–13]. The tungsten compounds are being extensively used in electrocatalysis due to the copious natural reserves and versatility in oxidation and coordination state of W, among other non-noble transition

\* Corresponding author.

\*\* Corresponding author at: Department of Nano Convergence Engineering (BK21 Four), Jeonbuk National University, Jeonju, Jeonbuk 54896, Republic of Korea.

E-mail addresses: [nhk@jbnu.ac.kr](mailto:nhk@jbnu.ac.kr) (N.H. Kim), [jhl@jbnu.ac.kr](mailto:jhl@jbnu.ac.kr) (J.H. Lee).

<https://doi.org/10.1016/j.apcatb.2023.122711>

Received 16 December 2022; Received in revised form 25 March 2023; Accepted 29 March 2023

Available online 30 March 2023

0926-3373/© 2023 Elsevier B.V. All rights reserved.

metals (TMs), in various forms like oxides, carbides, nitrides, sulfides, and selenides [14–16]. Selectively, tungsten oxide ( $\text{WO}_3$ ), a semi-conducting metal oxide (SMO), has attracted widespread attention toward the electrocatalytic HER and ORR activity due to its corrosion-resistant stable electronic structure, but still suffers in practical applicability owing to its languid electric conduction and lower OER prevalence [15,17]. Nevertheless, the efficiency of the electrocatalytic performance of  $\text{WO}_3$  is limited only to acidic electrolytes, larger bandgap, and in situ electrochemical reduction of  $\text{WO}_3$  to  $\text{WO}_{3-x}$  creating oxygen vacancy [18]. The electrocatalytic efficiency of  $\text{WO}_3$  in an alkaline medium is less studied due to stability issue however the electronic modulation of  $\text{WO}_3$  via defect engineering, interface structuring, composite assembly, etc. with a flexible coordination mode of W enhance the activity, selectivity, and stability during the electrocatalysis in alkaline electrolyte [15]. The  $\text{WO}_3$  in a single crystalline phase is highly affected in an alkaline medium and the maximum dissolution may occur during electrochemical processes and so the modification of tungsten lattice in  $\text{WO}_3$  by carbon to form  $\text{WO}_3$ -WC heterojunction as the catalyst support could be a promising pathway to establish a poised electrode [12]. For the purpose of art, the strategic conversion of the TMO into the transition metal carbide (TMCs) by a simple pseudomorphic carbonization process boosts the electrocatalytic behavior due to the ceramic properties, high conductivities, chemical durability, and summited thermal stability of metal carbides [19–21]. In outline, tungsten carbide (WC) is another appealing material possessing platinum-like d-electronic structure, high mechanical and chemical stability, strong resistance to electrocatalytic poisoning, vivid electronic conductivity, and hydrophilicity, which benefits have peaked its use in electrochemical HER, OER, and ORR [22,23]. Additional electrocatalytic active sites might be generated when the hexagonal  $\text{WO}_3$  is partially converted into the WC by clogging the carbon atoms in the interstitial sites of the crystal lattice [18,19]. As such, the multiple oxidation states of tungsten together with oxide–carbide interfaces boost the electrocatalytic efficiency for ORR, OER, and HER applications [17]. Yet another technique is the integration of multiple interfaces along with the choice of multi-component elemental composition, the coupling of two or more functional components with diverse properties, to obtain a structure that is remarkable to procure multifunctionality in the electrocatalyst [3,24]. A new class of electrocatalyst metal–organic frameworks (MOFs) have attracted the notion due to their innate porosity, structural tunability, compositional flexibility, open metal sites, and persistent metal–ligand active centers [25,26]. The Fe–MOFs and Cu–MOFs are truly active multifunctional electrocatalysts because of the redox-active metal center, and the good compatibility of the MOFs hybridized with bimetallic centers is the best way to integrate the respective merits of Fe and/or Cu-based MOFs [11,27,28]. Of special interest to construct new outstanding properties, Fe and Cu bimetallic paddlewheel units using benzene-1,3,5-tricarboxylate (BTC) linker might generate the coordinatively unsaturated metal sites, larger pores, and chemically stable geometry [29]. BTC is a bulky tritopic linker and an excellent candidate for the construction of mesoporosity, which is beneficial for mass transport, the creation of diffusion channels, and increase of the catalytic active sites [30].

Herein, we collocate all the mentioned possibilities to enrich the multitudinous electrochemical performances and synthesized a novel multi-interfacial dendritic FeCu–BTC/ $\text{WO}_3$ -WC ternary nanocomposite electrocatalyst by employing standard hydro/solvothermal and annealing processes. Our main motive was to create multiple interfaces through the heterojunctions to modulate the crystalline and geometric structure, tune the morphology, and modify the local coordination environment, as well as the electronic distribution, which has been demonstrated as a promising pathway to promote charge transfer and reactant exchange during electrochemical reactions. The approach of hetero-interface between the oxide–carbide and MOF is the first report to assume the interface bridges among the phases for electron transportation from the  $\text{WO}_3$ -WC interface, thus involving the HER and ORR

kinetics to reduce the adsorption–desorption energies, while the additional FeCu–BTC framework makes a mesoporous channel to transfer the reaction intermediates, thus improving the OER performance and the overall electrochemical activity of the catalyst (FeCu–BTC/ $\text{WO}_3$ -WC). Our approach of coupling the tungsten oxide–carbide active electrocatalyst with FeCu–BTC MOF ternary nanocomposite involves the multiple hetero-phases, which as a consequence, serves to boost the electrocatalytic activity through the: (a) atomic arrangements and electronic structure at the surfaces and/or interfaces, (b) electronic interaction and synergistic effect between the components, (c) modulation of the geometric and electronic structures, as well as the crystalline property, (d) redistribution of electrons around the interfaces promoting charge transfer, (e) bridging of the interfaces for electron transport, and (f) optimal electrocatalysis due to electronic interaction to balance the adsorption–desorption behavior of the reactant and catalyst [14,24]. Therefore, rational design of the heterostructures catalysts with multiple interfaces and abundant active sites simultaneously improves the OER, HER, and ORR performance, thus asserting the practical demands of Zn–air batteries and water-splitting electrolyzer.

## 2. Experimental

### 2.1. Synthesis of $\text{WO}_3$ –WC nanorods

A hydrothermal incubation followed by annealing technique was adopted for the synthesis of  $\text{WO}_3$ -WC nanorods. Typically, 5 mmol of  $\text{Na}_2\text{WO}_4 \cdot 2\text{H}_2\text{O}$  was dissolved in 20 mL DI water to form a clear solution. The 3 M HCl solution prepared separately was then added dropwise in a continuously stirring solution to adjust the pH to  $\sim 1.2$ , where a pale-yellow transparent solution formed. In the meantime, 15 mmol  $\text{H}_2\text{C}_2\text{O}_4$  and 1 g  $(\text{NH}_4)_2\text{SO}_4$  were dissolved separately in 10 mL DI water each and were subsequently dripped into the vigorously stirred solution. For the next step, 0.5 g glucose dissolved in 5 mL water by ultrasonication was mixed with the above mixture solution, and continuous stirring was maintained for a further 2 h. Then, the volume of mixture solution was made up to 60 mL by adding DI water, and transferred into 100 mL PTFE-lined tubes, and sealed in stainless steel autoclave. The reaction was set aside in a hot air oven at 180 °C for 16 h. Once the reaction was complete and the autoclaves cooled to room temperature (RT), the as-synthesized product was retrieved by centrifugation, and washed with water and ethanol. The solid powder was then dried in a vacuum oven at 60 °C for 12 h. Finally, the white powder obtained was heated in a tube furnace at 850 °C for 2 h under continuous flow of  $\text{H}_2/\text{Ar}$  (10%  $\text{H}_2$ ) gas. The black  $\text{WO}_3$ -WC powder was then stored in an incubator for further use [31,32]. For the synthesis of pure  $\text{WO}_3$ , the same synthetic protocol was adopted, except the glucose precursor.

### 2.2. Synthesis of FeCu–BTC/ $\text{WO}_3$ -WC

For the synthesis of the FeCu–BTC MOF nanonetwork on  $\text{WO}_3$ -WC nanorods, 0.5 g  $\text{H}_3\text{BTC}$ , 0.5 mmol  $\text{Cu}(\text{NO}_3)_2 \cdot 3\text{H}_2\text{O}$ , and 0.5 mmol  $\text{Fe}(\text{NO}_3)_3 \cdot 9\text{H}_2\text{O}$  were fully dispersed in 50 mL solvents (DMF: ethanol: water; 20 mL: 20 mL: 10 mL). Then, 200 mg of the prepared  $\text{WO}_3$ -WC powder was poured into the solution mixture and stirred vigorously for 2 h. Next, the resulting solution was transferred to 100 mL PTFE lined tubes and sealed in stainless steel autoclave. The reaction was incubated in hot air oven at 120 °C for 5 h under autogenous pressure. After that, the solution was allowed to cool naturally to RT. Then, the product was separated by centrifugation, and washed several times with ethanol and water. Finally, the FeCu–BTC/ $\text{WO}_3$ -WC was obtained by drying the product at 60 °C in a vacuum oven for 12 h. The sample obtained was stored in an incubator for further use.

### 2.3. Synthesis of FeCu–BTC

First, 0.5 g  $\text{H}_3\text{BTC}$ , 0.5 mmol  $\text{Cu}(\text{NO}_3)_2 \cdot 3\text{H}_2\text{O}$ , and 0.5 mmol  $\text{Fe}$

( $\text{NO}_3$ )<sub>3</sub>·9 H<sub>2</sub>O were fully dispersed in 50 mL solvents (DMF: ethanol: water; 20 mL: 20 mL: 10 mL) in bath sonication. The clear reaction mixture was then transferred to 100 mL PTFE lined tubes, sealed in stainless steel autoclave, and heated in hot oven at 120 °C for 5 h. Once the solution cooled naturally to RT, the sample was collected by centrifugation, followed by washing several times with water and ethanol. Finally, FeCu-BTC powder sample was obtained by drying the product at 60 °C in a vacuum oven for 12 h. The sample obtained was stored in an incubator for further use.

#### 2.4. Preparation of commercial Pt-C/RuO<sub>2</sub> catalyst ink

The commercial Pt-C and RuO<sub>2</sub> powders (4.8 mg) were separately fully dispersed in 350  $\mu\text{L}$  DI water, 250  $\mu\text{L}$  polyvinyl alcohol, and 10  $\mu\text{L}$  Nafion. The mixture was sonicated for 30 min in bath sonication to obtain a homogeneous ink suspension. The catalyst ink was then used for the subsequent electrochemical test [33].

#### 2.5. Electrode preparation

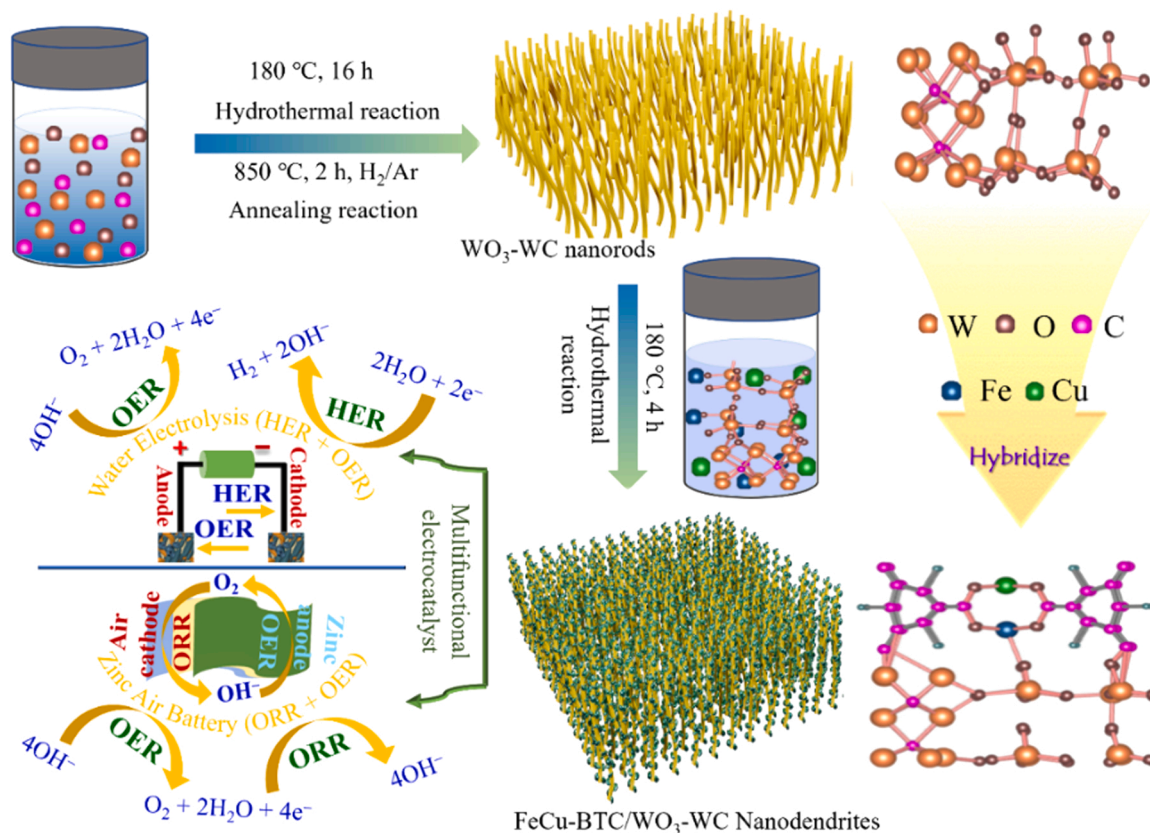
The catalyst ink was prepared using the usual polymer binder method. The electrocatalyst material was weighed (~10 mg) separately, and dispersed in 350  $\mu\text{L}$  DI water, 250  $\mu\text{L}$  polyvinyl alcohol, and 10  $\mu\text{L}$  Nafion by sonication for 30 min. For HER, OER, and alkaline water electrolyzer, a pre-cleaned 1 cm  $\times$  1 cm bare Ni foam was homogeneously coated with the catalyst ink and dried in a vacuum oven for use as working electrode. For ORR, an optimum amount of catalyst ink (~400  $\mu\text{g}/\text{cm}^2$ ) was dropped into the RDE and dried in ambient air. For aqueous ZAB, the catalyst ink (~5  $\text{mg}/\text{cm}^2$ ) was drop cast in an air-diffusing carbon cloth.

### 3. Result and discussion

#### 3.1. Material synthesis, crystallography, and spectroscopic analysis

Scheme 1 illustrates a lucid and eloquent nanofabrication process intended for the FeCu-BTC/WO<sub>3</sub>-WC electrocatalyst via a two-step hydro/solvothermal reaction, followed by quenching. First, the WO<sub>3</sub> nanorods primarily composed of the optimum carbon source were synthesized using a typical hydrothermal reaction at 180 °C. A controlled heat treatment pseudomorphic transformation synthesis protocol to fabricate highly crystalline WO<sub>3</sub>-WC nanorods in tube furnace using Ar carrier gas and H<sub>2</sub> reductant was adopted to achieve superior morphological retention together with a unique oxide-carbide heterophase [32]. In contrast, the previous literature studied substantial morphological changes in longer reaction time and fascinated by the in situ reduction/carbonization process, the WO<sub>3</sub> was initially reduced into the WO<sub>3-x</sub> creating the oxygen vacancy, and at higher temperature, carbon atoms covalently bonded with W<sup>4+</sup> ions to form WC. Unlike the conventional nanomaterials and inspired by the outstanding electrocatalytic performance of a multi-interfacial concoction along with a twinning electrochemical stability, we were interested in a second-step hydro-solvothermal reaction with a highly exploited MOF moiety having multiple coordinating spots, and the WO<sub>3</sub>-WC nanorods were then entwined with the FeCu-BTC (more detail in the experimental section). Interestingly, with this casual synthetic strategy, we sought to conceptualize the electronic coupling of the highly stable oxide-carbide matrix with the surface overlayer of another highly catalytically active bimetallic MOF ensemble for the first time as a multifunctional electrocatalyst.

The powder X-ray diffraction (PXRD) study of the as-synthesized electrocatalyst was conducted to assure the crystal structure and multi-interfacial phases (Fig. 1a). The Bragg angles of (22.05, 23.69,



**Scheme 1.** Schematic of the synthesis of dendritic FeCu-BTC/WO<sub>3</sub>-WC nanocomposite electrocatalyst and its application in the zinc-air battery and water-splitting electrolyzer.



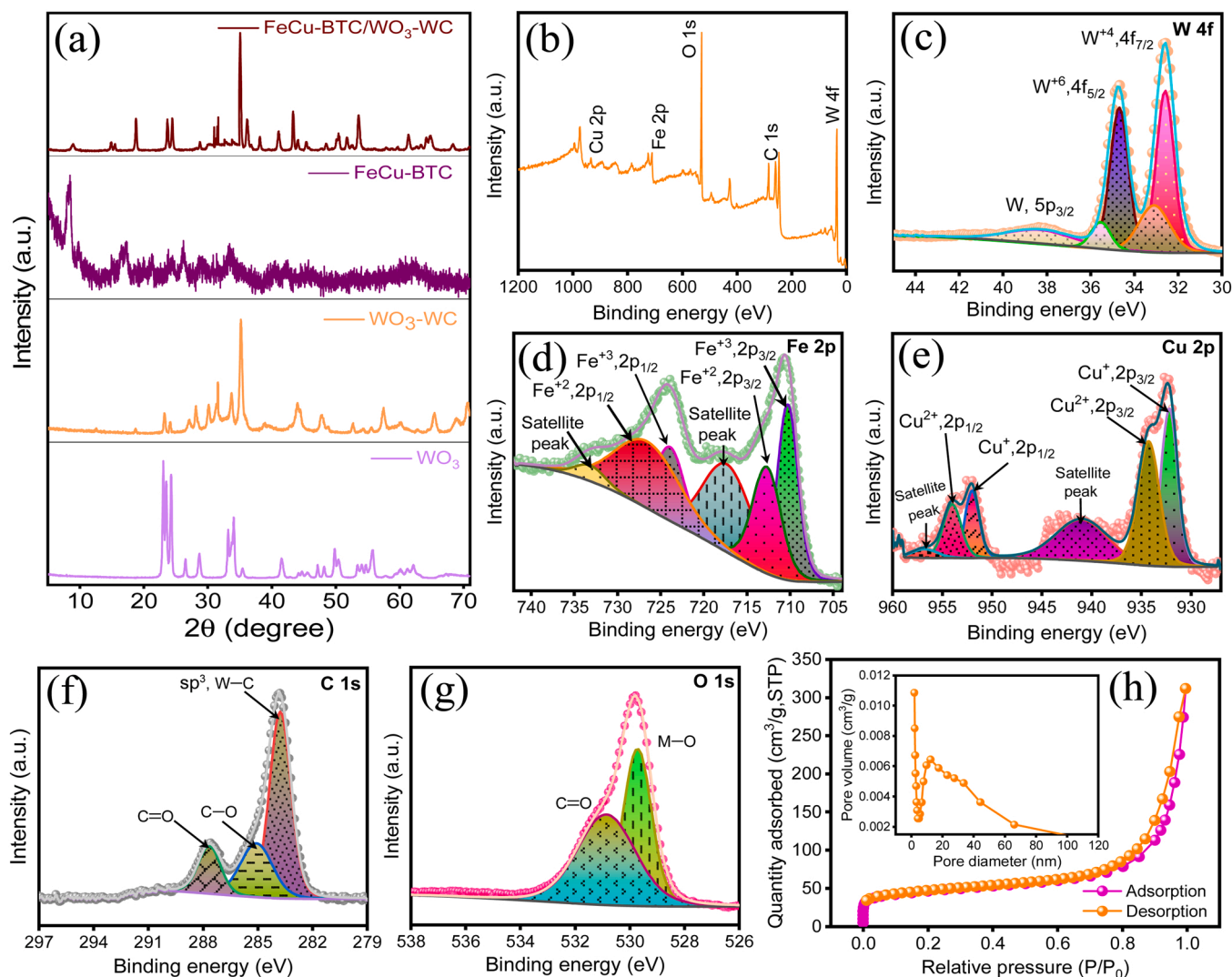


**Fig. 1.** (a) XRD patterns of the WO<sub>3</sub>, WO<sub>3</sub>-WC, FeCu-BTC, and FeCu-BTC/WO<sub>3</sub>-WC. Deconvoluted fitted HR- XPS spectra of the (b) survey, (c) tungsten (W 4 f), (d) iron (Fe 2p), (e) copper (Cu 2p) (f) carbon (C 1 s), and (g) oxygen (O 1 s). (h) Nitrogen sorption study of the FeCu-BTC/WO<sub>3</sub>-WC (inset: BJH pore size distribution curve of the FeCu-BTC/WO<sub>3</sub>-WC).

24.11, 26.53, 28.77, 33.23, 33.61, 34.05, 41.49, 47.19, 49.30, and 55.41°, corresponding to the (001), (020), (200), (120), (111), (021), (201), (220), (221), (002), (400), and (420) crystalline planes, respectively, designate the orthorhombic WO<sub>3</sub> nanorods (JCPDF no. 20-1324) [13,18,34]. Similarly, the additional intense peaks at  $2\theta$  = (31.44, 35.62, and 48.26)° are sternly indexed to the (001), (100), and (101) crystal planes, respectively, of the hexagonal WC (JCPDF no: 51-0939), thus representing the formation of the WO<sub>3</sub>-WC crystal interface (Fig. 1a) [35]. The characteristic Bragg diffraction peaks at  $2\theta$  = (8.5, 14.9, 17.18, 26.12, and 33.18)° are ascribed to the formation of the bimetallic FeCu-BTC MOF crystal phase reported elsewhere (Fig. 1a) [36,37]. Moreover, the crystal structure of FeCu-BTC/WO<sub>3</sub> catalyst was assured (Fig. S1, Supporting Information) where the prominent diffraction peaks at lower  $2\theta$  value correspond to the FeCu-BTC is in good agreements with the previous study of metal-BTC MOF and additional characteristic peaks representing the orthorhombic WO<sub>3</sub> (JCPDF no. 20-1324) [34,37]. Overall, the formation of the multi-interfacial crystalline nanostructure of FeCu-BTC integrated on WO<sub>3</sub>-WC is established (Fig. 1a).

The chemical states of the constituent elements present in the electrocatalysts were evaluated by high-resolution X-ray photoelectron spectroscopy (HR-XPS) study. The electronic state of individual

elements and their interaction in composites were concurrently interrogated. The W 4f in WO<sub>3</sub>-WC catalysts (Fig. S2a, Supporting Information) were first fitted into 4 deconvoluted peaks, a pair of peaks at 32.08 and 34.18 eV ascribed to W<sup>+4</sup> (4f<sub>7/2</sub> and 4f<sub>5/2</sub> respectively) while a pair of distinct peaks at 35.88 and 37.98 eV attributes W<sup>+6</sup> (4f<sub>7/2</sub> and 4f<sub>5/2</sub> respectively) representing W-C and W-O chemical bond [38]. A sharp peak at 284.02 eV for deconvoluted C 1s represents W-C bond and oxygen containing carbonaceous bond (C-O) at binding energy 285.28 eV (Fig. S2b, Supporting Information) in WO<sub>3</sub>-WC [23]. The W-O bond formations is confirmed from a characteristic O 1s peak at 530.48 eV representing surface structure of WO<sub>3</sub> (Fig. S2c, Supporting Information) also sorting presence of lattice C-O (531.78 eV) bond. These results verify the presence of prominent W-O and W-C chemical bonds confirming the formation of WO<sub>3</sub>-WC nanorods heterostructure [21]. Similarly, Fig. S3, Supporting Information depicts the XPS results of FeCu-BTC MOF catalyst. The Fe 2p spectrum (Fig. S3a, Supporting Information) with binding energy peaks at 710.38 eV (Fe<sup>+3</sup>, 2p<sub>3/2</sub>), 724.33 eV (Fe<sup>+3</sup>, 2p<sub>1/2</sub>), 712.88 eV (Fe<sup>+2</sup>, 2p<sub>3/2</sub>), 727.66 eV (Fe<sup>+2</sup>, 2p<sub>1/2</sub>), 717.88 & 734.28 eV (satellite) genuinely forecast the multivalent state of Fe in FeCu-BTC [39]. Further analysis on Cu 2p deconvoluted peaks indicate the monovalent Cu ions at 933.08 eV (2p<sub>3/2</sub>), 752.88 eV (2p<sub>1/2</sub>), divalent Cu ions at 934.38 eV (2p<sub>3/2</sub>), 953.96 eV



( $2p_{1/2}$ ), and the satellite peaks at 942.98 & 962.78 eV (Fig. S3b, Supporting Information) [40]. The BTC MOF in catalyst were declared from C 1 s deconvoluted XPS peak analysis ensuring three prominent spectra at binding energy of 284.48 eV standing for C-C/C=C bond, 286.08 eV for C-O bonds, and 287.38 eV regarding C=O bonds (Fig. S3c, Supporting Information) [41]. Additionally, the Fig. S3d, Supporting Information confirms the presence of dominant M-O bond at 531.18 eV and carbonaceous C=O bond at 533.78 eV in the O 1 s XPS spectrum [30,42]. Fig. 1b shows the comprehensive XPS survey spectra for collective elemental composition that reveals the presence of Fe, Cu, W, O, and C elements based on the semi-quantitative analysis of XPS for FeCu-BTC/WO<sub>3</sub>-WC electrocatalyst. The deconvoluted XPS fitting peaks of W 4 f (Fig. 1c) at 32.5 and 33.6 eV are attributed to the W-C bonds ( $W^{+4}$ ,  $4f_{7/2}$ ), while the peaks located at (34.5 and 35.8) eV represent the formation of the W-O bonds of WO<sub>3</sub> ( $W^{+6}$ ,  $4f_{5/2}$ ) [19,43]. The minor peak at 38.1 eV signifies the  $W^{+6}$ ,  $5p_{3/2}$  [34]. The HR-XPS spectra of Fe 2p of the FeCu-BTC/WO<sub>3</sub>-WC sample shown in Fig. 1d discloses the Fe<sup>+3</sup> valence state of iron situated at 710.1 ( $2p_{3/2}$ ) and 723.3 eV ( $2p_{1/2}$ ) and the Fe<sup>+2</sup> valence state of iron at 712.8 ( $2p_{3/2}$ ) and 727.1 eV ( $2p_{1/2}$ ) respectively, whereas the additional two satellite shake-up peaks for metallic Fe 2p at higher binding energy at 717.5 and 737.2 eV indicate the strong ligand metal charge transfer from Fe sites [25,29]. Analysis of the Cu 2p spectrum (Fig. 1e) reveals the characteristic XPS peak of the Cu<sup>+2</sup> oxidation state at binding energy 934.4 and 953.9 eV, and the presence of monovalent Cu ( $Cu^{+1}$ ) at (932.1 and 952.1) eV, specifying the presence of lower oxidation state of Cu, demonstrating the ease of electron transfer [11,30]. Similarly, the satellite shake-up peaks of Cu at 940.8 and 956.5 eV assert the strong configuration interaction and assignment of chemical states (Fig. 1e) [30]. The different bonding state of carbon in FeCu-BTC/WO<sub>3</sub>-WC sample was analyzed by the deconvoluted C 1 s peaks (Fig. 1f). The  $sp^3$  carbon in the W-C bond at 283.8 eV implies the formation of tungsten carbide, and the additional C-O (285.1 eV), C=O (287.5 eV) peaks grimly explain about the carboxylate moiety of BTC MOF linker [30,44]. The duplet peaks at (530.05 and 531.8) eV for (M-O) and (C=O) correspond to the O 1 s signal, which represents the formation of WO<sub>3</sub> and the oxygen-rich environment in the material, due to the integration of BTC MOF (Fig. 1g) [11,30]. As can be seen from the results discussed above, small binding energy shift in the core level spectra of multi-component catalyst (FeCu-BTC/WO<sub>3</sub>-WC) from that of WO<sub>3</sub>-WC or FeCu-BTC catalyst signifies the charge transfer behavior between the elements during hetero-phase formation, an indicative of change in chemical environment [45]. More importantly, the small positive shift in BE of Fe 2p (~0.18 eV) and negative shift of BE of Cu 2p (~0.9 eV) in FeCu-BTC/WO<sub>3</sub>-WC from FeCu-BTC manifests the partial transfer of electron between Fe and Cu through O-bridge in ligand, referring positive influence on catalysis reactions [46]. The comprehensive XPS analysis of the corresponding elements and their respective chemical states of the FeCu-BTC/WO<sub>3</sub>-WC sample confirms the formation of bimetallic FeCu-BTC MOF integrated with the WO<sub>3</sub>-WC nanorods.

### 3.2. Specific surface area, porosity, and microscopic structural analysis

For electrocatalytic multifunctionality, specific surface area, as well as the textural porosity of the material, is utmost [47]. Thus, the N<sub>2</sub> sorption analyses were used to measure the pore size distribution, and are presented in Fig. 1h, and S4, Supporting Information. The electrocatalysts WO<sub>3</sub>, WO<sub>3</sub>-WC, FeCu-BTC, FeCu-BTC/WO<sub>3</sub> (Fig. S4a, Supporting Information), and FeCu-BTC/WO<sub>3</sub>-WC (Fig. 1h) showed the relaying of the IV-type Brunauer–Deming–Deming–Teller (BDDT) isotherm model, the H<sub>3</sub>-type hysteresis loop in the (0–1) P/P<sub>0</sub> pressure range, and simultaneously indicate the presence of bimodal meso-structural configuration [19]. As shown by the N<sub>2</sub> sorption analysis, the calculated Brunauer–Emmett–Teller (BET) surface area of the electrocatalyst FeCu-BTC/WO<sub>3</sub>-WC, FeCu-BTC/WO<sub>3</sub>, WO<sub>3</sub>-WC, and WO<sub>3</sub> was found to be (156.30, 117.84, 76.72, and 56.28) m<sup>2</sup>g<sup>-1</sup>, respectively

(Fig. 1h, and S4a, Supporting Information). Hierarchical assembly of the WO<sub>3</sub>-WC nanorods with FeCu-BTC nanodiamonds composite results in a highest surface area dendritic nanoconfiguration with significantly higher pore diameter (12.44 nm, inset of Fig. 1h) for FeCu-BTC/WO<sub>3</sub>-WC and the mesoporous property [31]. The Barrett–Joyner–Halenda (BJH) pore size distribution of all samples (inset of Fig. 1h, and S4b, Supporting Information) clearly illustrates the formation of plentiful nanopores in the range 3–100 nm. The multiple porous feature and high porosity in the electrocatalyst can effectively enrich the active contact area of electrode–electrolyte, reduce the diffused resistor, and facilitate a prompt electrochemical reaction [16].

The structural prosperity of the WO<sub>3</sub>, WO<sub>3</sub>-WC nanorods and the hybrid FeCu-BTC/WO<sub>3</sub>-WC nanocomposites were analyzed by the field emissions scanning electron microscopic (FE–SEM) and the transmission electron microscopic (TEM) images. The initial FE–SEM images of WO<sub>3</sub> (Fig. 2a & b) show the straight and smooth surface nanorods. Individual nanorods of WO<sub>3</sub> are aligned vertically, and gradually sharpen towards the tip (Fig. 2b). The FE–SEM images in Fig. 2c & d are genuine indications of the pseudomorphic transformation of WO<sub>3</sub> with utmost morphological retention, leading to the formation of WO<sub>3</sub>-WC by controlled heat treatment to accomplish the unique oxide–carbide heterophase. Typical FE–SEM images of the FeCu-BTC/WO<sub>3</sub>-WC nanocomposites (Fig. 2e & f) conjures randomly distributed nanodiamond units of FeCu-BTC MOF in conjunction with WO<sub>3</sub>-WC nanorods, thus forming highly interconnected nanodendritic branches. A close inspection of the FeCu-BTC/WO<sub>3</sub>-WC nanocomposite (Fig. 2f) clearly projects the different sized nanodendritic architectonics of oxide–carbide and MOF envision the larger surface area and enormous porosity (Fig. 1h), integrated branch chain structure, and high-index exposed multiple facets. Also, the FE–SEM energy dispersive X-ray spectroscopic (FESEM–EDS) images (Fig. S5a–f, Supporting Information) and FESEM–EDS spectrum (Fig. S5g, Supporting Information) clearly reveal the microstructural elemental distribution and the presence of all the individual elements (W, O, C, Fe, Cu) in FeCu-BTC/WO<sub>3</sub>-WC. Thus, the dendritic nanoarchitectonics of the FeCu-BTC/WO<sub>3</sub>-WC facilitates the contact between active sites and electrolyte due to the presence of a significant number of catalytically active atoms at the edges and corners, thus shortening the mass diffusion pathways for intensive electrocatalytic activity [9]. Furthermore, the transmission electron microscopy (TEM) images, high-resolution TEM (HR–TEM) images, scanning transmission electron microscopy (STEM) images, and the elemental composition collected as maps in STEM images (STEM–EDS) of WO<sub>3</sub>, WO<sub>3</sub>-WC (Fig. S6, Supporting Information) clearly indicate the formation of nanorods, as depicted in the FESEM images of Fig. 2a–d. A more claritive illustration of the formation of dendritic structure consisting of interconnected bunches of multidimensional nanorods and nanodiamonds was obtained from the TEM image of the FeCu-BTC/WO<sub>3</sub>-WC nanocomposites (Fig. 2g & h). The well-defined dendritic nanostructure as obtained in the magnified TEM (Fig. 2h) images shows the crystal orientation of the central nanorods and the aligned nanodiamonds. Meanwhile, the high-resolution TEM (HR–TEM) images (Fig. 2i) at the edges of the nanorods show clear heterointerfaces between the crystalline WO<sub>3</sub>, WC, and the FeCu-BTC. The fast Fourier transform (FFT, inset; Fig. 2i) and the inverse fast Fourier transform (IFFT, Fig. 2j) obtained from the region X in Fig. 2i also confirm the formation of heterointerfaces, crystal mismatch entailing the lattice fringes with d-spacing of 0.38 nm corresponding to the (001) plane of WO<sub>3</sub> and 0.25 nm corresponding to the (100) plane of WC. No obvious crystal planes are assigned for the pristine FeCu-BTC MOF, but the high-angle annular dark-field STEM (HAADF–STEM) images (Fig. 2k) explore the atomic resolution of the FeCu-BTC/WO<sub>3</sub>-WC nanodendrite, showing spotted lattices (green circles) of WO<sub>3</sub> (0.369 nm for the 200 plane), spotted lattices (green box) of WC (0.252 nm for the 100 plane), along with the conspicuous FeCu–MOF heterojunction. The STEM–EDS elemental mapping (Fig. 2l & m<sub>1</sub>–m<sub>6</sub>), EDS spectra (Figure 2m<sub>7</sub>), and line profile (Fig. S7, Supporting

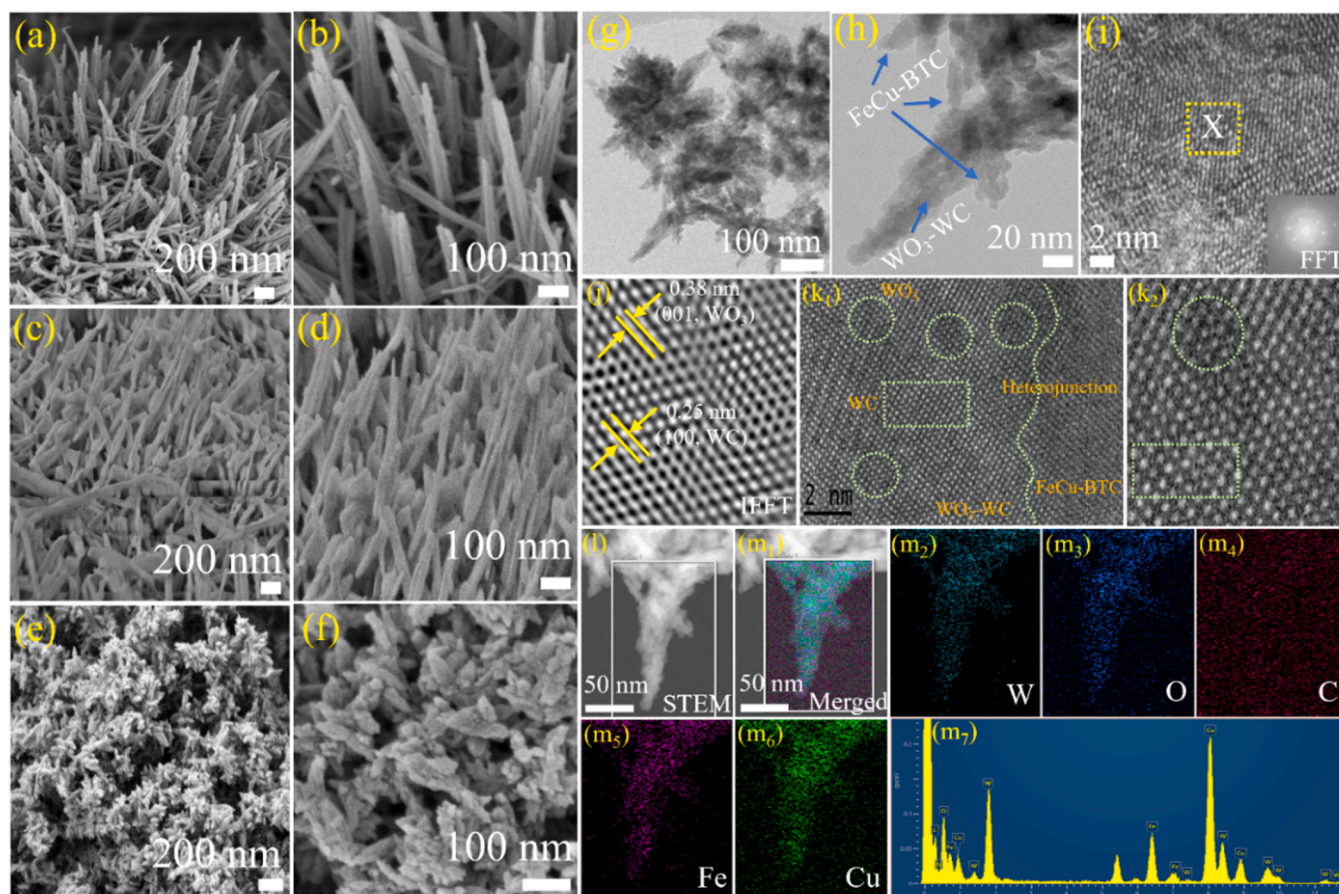


**Fig. 2.** FE-SEM images showing the microstructure of (a–b)  $\text{WO}_3$  nanorods, (c–d)  $\text{WO}_3$ -WC nanorods, and (e–f) FeCu-BTC/ $\text{WO}_3$ -WC dendritic nanostructures from lower to higher magnification. TEM images of (g–h) FeCu-BTC/ $\text{WO}_3$ -WC. HR-TEM images of (i) FeCu-BTC/ $\text{WO}_3$ -WC (inset: FFT image). (j) IFFT patterns derived from region X in Fig. 2i. (k) High-angle annular dark-field scanning transmission electron microscopy (HAADF-STEM) image of the FeCu-BTC/ $\text{WO}_3$ -WC. (l) STEM image of the FeCu-BTC/ $\text{WO}_3$ -WC. STEM-EDS-based elemental color mapping of FeCu-BTC/ $\text{WO}_3$ -WC showing constituent elements of (m<sub>1</sub>) merged, (m<sub>2</sub>) tungsten, (m<sub>3</sub>) oxygen, (m<sub>4</sub>) carbon, (m<sub>5</sub>) iron, and (m<sub>6</sub>) copper. STEM-based elemental distribution in (m<sub>7</sub>) EDS spectrum.

**Information**) images show the uniform distribution of the W, O, C, Fe, and Cu elements in the FeCu-BTC/ $\text{WO}_3$ -WC nanodendrite. The microstructural and quantitative analysis of FeCu-BTC/ $\text{WO}_3$ -WC nanocomposite convincingly shows that the highly coupled nanodendritic heterostructures with tunable porosity and surface area efficiently boost the electrocatalytic HER, OER, and ORR processes, thus facilitating the water electrolysis and Zn-air battery performances.

### 3.3. Electrocatalytic reaction study

The cogent physicochemical characteristics of the FeCu-BTC/ $\text{WO}_3$ -WC dendritic hetero-nanojunction prompt evaluation of the multifunctional electrocatalytic activities towards HER, OER, ORR, zinc air battery (ZAB), and alkaline water electrolysis. The catalyst ink of the powder samples of FeCu-BTC/ $\text{WO}_3$ -WC, FeCu-BTC/ $\text{WO}_3$ ,  $\text{WO}_3$ -WC,  $\text{WO}_3$ , commercial Pt-C, and  $\text{RuO}_2$  were prepared for electrocatalytic reaction study (details in the experimental section). The three-electrode electrolytic cell system consisting of 1 cm × 1 cm catalyst-loaded Ni foam working electrode, Ag/AgCl reference electrode, and graphite rod counter electrode in 1 M KOH was set up for electrocatalytic HER and OER study. A coupled symmetric two-electrode system in 1 M KOH electrolyte was configured for overall alkaline water splitting study. The ORR study was investigated through a glassy carbon rotating disk electrode (RDE) loaded with catalyst ink as a working electrode, Ag/AgCl reference electrode, and graphite rod counter electrode in 0.1 M KOH solution. The self-made aqueous zinc air cell constructed with catalyst ink drop cast in an air-diffusing carbon cloth as air cathode and

Zn plate as air anode (details in supporting information) was used for ZAB performances.

To draw up the initial intrinsic electrocatalytic activity of the synthesized catalysts, an effective quantitative approach to generalize the active surface area of electrocatalysts calculated from the double layer capacitance ( $C_{dl}$ ) is proxy for electrochemically active surface area (ECSA) and the overall electrochemical reactions [48]. For this, the current responses were recorded by the cyclic voltammetry (CV) in a non-Faradaic potential region of (1.125 – 1.225) V vs. RHE at a scan rate ranging (20 – 140) mV s<sup>−1</sup> (Fig. S8, Supporting Information) and the difference of the cathodic-anodic current as a function of scan rate revealed a linear function where the slope indicates the  $C_{dl}$  (detailed calculation in the experimental section). The corresponding  $C_{dl}$  values obtained as FeCu-BTC/ $\text{WO}_3$ -WC (29.6 mV dec<sup>−1</sup>), FeCu-BTC/ $\text{WO}_3$  (26.9 mV dec<sup>−1</sup>), FeCu-BTC (18.3 mV dec<sup>−1</sup>),  $\text{WO}_3$ -WC (15.6 mV dec<sup>−1</sup>), and  $\text{WO}_3$  (12.1 mV dec<sup>−1</sup>) with ECSA value of (740, 672.5, 457.5, 390, and 302.5) m<sup>2</sup>g<sup>−1</sup>, respectively (Fig. S8, Supporting Information). In this regard, the enhanced electroactivity of the dendritic FeCu-BTC/ $\text{WO}_3$ -WC compared to that of the other counterparts can be attributed to the highly interconnected multiple heteronanojunctions with patterned architecture, which ultimately results in the high ECSA, and the efficient mass transfer [49]. The good accord of the highly porous hierarchical FeCu-BTC/ $\text{WO}_3$ -WC nanodendritic structure with high BET surface area (depicted from sorption analysis, Fig. 1j) with the electrochemical surface area improves the mass diffusion during electrochemical reactions, promoting the electron transfer process.



### 3.3.1. Bifunctional oxygen electrocatalysis (ORR and OER) study

The bifunctional oxygen electrocatalysis for ORR and OER is crucial for the immanent application in rechargeable metal air battery and regenerative fuel cell technology. The fascinating morphological

assortment and the multiple hetero-nanointerfaces in dendritic FeCu-BTC/WO<sub>3</sub>-WC electrocatalyst prompted evaluation of the oxygen bifunctional electrocatalysis performances. For this, the ORR catalytic activity of the FeCu-BTC/WO<sub>3</sub>-WC nanocomposite was initially

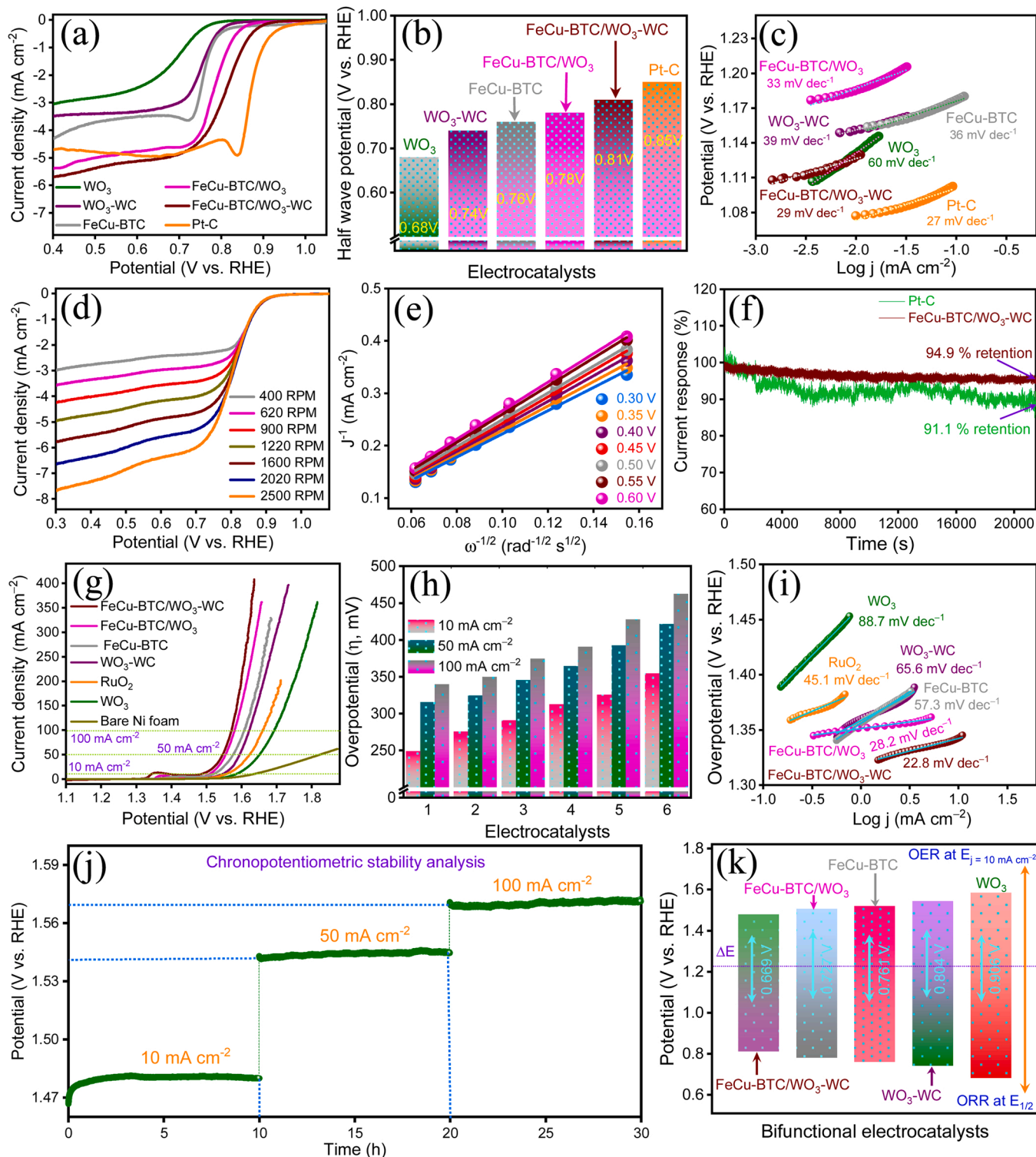


**Fig. 3.** Oxygen electrocatalysis (ORR and OER) study: (a) LSV polarization curves for ORR. (b) Bar diagram showing the half-wave potential of the electrocatalysts. (c) Corresponding Tafel plots and Tafel slope values of the electrocatalysts. (d) ORR polarization curves of the FeCu-BTC/WO<sub>3</sub>-WC at rotating rates from (400 – 2500) rpm. (e) K–L plots of the FeCu-BTC/WO<sub>3</sub>-WC based on Fig. 3d at different potentials. (f) Chronoamperometric stability report of the FeCu-BTC/WO<sub>3</sub>-WC and commercial Pt-C. (g) LSV polarization curves for OER. (h) Bar diagram showing the overpotential of the electrocatalysts at (10, 50, and 100) mA cm<sup>-2</sup> current density. (i) Corresponding Tafel plots and Tafel slope values of the electrocatalysts. (j) Chronopotentiometric stability analysis of the FeCu-BTC/WO<sub>3</sub>-WC at different overpotentials. (k) Corresponding potential gaps between the E<sub>1/2</sub> of ORR and η<sub>10</sub> of OER.



analyzed via CV measurement in O<sub>2</sub>- and N<sub>2</sub>-saturated 0.1 M KOH solution in a three-electrode set up at a scan rate of 5 mV s<sup>-1</sup>. Fig. S9 of the SI plots the results obtained, which show well defined cathodic peaks at around 0.81 V vs. RHE in O<sub>2</sub>-saturated 0.1 M KOH solution signaling the oxygen reduction process, while those in the N<sub>2</sub>-saturated 0.1 M KOH show practically negligible reduction of oxygen, implying the practicality of the FeCu-BTC/WO<sub>3</sub>-WC as a potential ORR active electrocatalyst [16]. The linear sweep voltammograms (LSV) are then measured using rotating disk electrode (RDE) at a rotating speed of 1600 rpm, and the polarization curves are plotted in Fig. 3a. The ORR catalytic activity of the different electrocatalysts was assessed based on their half-wave potential ( $E_{1/2}$ ), and capability of the electrocatalysts in reducing the ORR overpotential [28]. Fig. 3a & b outframe a notion about the ORR activity of FeCu-BTC/WO<sub>3</sub>-WC with significant half-wave potential (0.81 V vs. RHE) value, which is very close to the benchmark Pt-C catalyst ( $E_{1/2}$ =0.85 V vs. RHE) suggesting the excellent catalytic ORR activity. Similarly, the FeCu-BTC/WO<sub>3</sub>, FeCu-BTC, WO<sub>3</sub>-WC, and WO<sub>3</sub> as-prepared catalysts were also inspected for their ORR activities in response to their half-wave potential, and determined as: (0.78, 0.76, 0.74, and 0.68) V vs. RHE, respectively, showing relatively inferior ORR catalytic behavior to that of the FeCu-BTC/-WO<sub>3</sub>-WC. The superior catalytic activity of FeCu-BTC/WO<sub>3</sub>-WC can be attributed to the presence of ORR-active FeCu-MOF multicarboxylate linkers, porous carbon matrix capable of transporting ORR species (e<sup>-</sup>, H<sup>+</sup>/OH<sup>-</sup>, O<sub>2</sub>, and H<sub>2</sub>O) regulating the electrocatalytic performance, along with the synergistic influence of the conductive WO<sub>3</sub>-WC nanorods with abundant active sites in the dendritic hetero-nanointerfaces [28,43]. The superiority of the FeCu-BTC/WO<sub>3</sub>-WC catalyst towards the ORR process (Fig. 3c) can also be corroborated by the electro-kinetic Tafel slope value of 29 mV dec<sup>-1</sup>, a linear relation of the electrode potential and log of the current. The Tafel slopes (Fig. 3c) of the other FeCu-BTC/WO<sub>3</sub>, FeCu-BTC, WO<sub>3</sub>-WC, and WO<sub>3</sub> electrocatalysts are computed to be (33, 36, 39, and 60) mV dec<sup>-1</sup>, respectively. It is worth noting that the analogous Tafel slope value of FeCu-BTC/WO<sub>3</sub>-WC to that of the benchmark Pt-C catalyst of 27 mV dec<sup>-1</sup> indicates the practical ORR reaction kinetics, due to the high porosity and profuse O<sub>2</sub> chemisorption electroactive sites of these intriguing heterometals ensembles [38]. Furthermore, the kinetic parameters for ORR were also evaluated by the rotation rate dependence of the voltammograms for the reduction of O<sub>2</sub> in 0.1 M KOH for FeCu-BTC/WO<sub>3</sub>-WC at the rotation rate ranging (400–2500) rpm [35]. Fig. 3d shows that the shape and magnitude of the reduction current are entirely based on the rate of rotation, indicating the diffusion of the oxygen to the surface of catalyst and increased kinetics of the interfacial redox reactions [38]. The corresponding Koutechy-Levich (K-L) plots (Fig. 3e) for the FeCu-BTC/-WO<sub>3</sub>-WC in the potential range (0.3 – 0.6) V show the excellent linearity and parallelism, assigning the first-order reaction kinetics during the ORR process. The average electron transfer number ( $\bar{n}$ ) per oxygen molecule during the electrocatalytic ORR process calculated from the slope of the K-L plot is 3.89, indicating a most concurring direct reduction of oxygen to hydroxide reaction pathway via the four electron transfer [16]. The accelerated durability test (ADT) of the as-synthesized dendritic FeCu-BTC/WO<sub>3</sub>-WC nanocomposite and the commercial Pt-C catalyst was carried out to evaluate the durability of the ORR catalysis by long-term chronoamperometric stability test. The results obtained with continuous irradiation of constant potential for more than 20,000 s (Fig. 3f) for the FeCu-BTC/WO<sub>3</sub>-WC nanocomposite show excellent current responses with the loss of only 5.1% (94.9% retention) degradation while the commercial Pt-C showed continuous degrading current loss of around 8.9% (91.1% retention) for the same interval of time, demonstrating the high stability of the nanohybrid composite of FeCu-BTC/WO<sub>3</sub>-WC. All the discussion and analysis of the as-synthesized FeCu-BTC/WO<sub>3</sub>-WC hybrid nanocatalyst realizes a prospective application in the air cathodes of metal-air battery and/or fuel cell devices that is commercially competitive with the recently reported ORR electrocatalyst (Table S1, Supporting Information).

The OER catalytic performance of the FeCu-BTC/WO<sub>3</sub>-WC hybrid nanocatalyst was evaluated via a three-electrode set-up in N<sub>2</sub>-saturated 1 M KOH. For comparison, commercial RuO<sub>2</sub>, FeCu-BTC/WO<sub>3</sub>, FeCu-BTC, WO<sub>3</sub>-WC, WO<sub>3</sub>, and the bare Ni foam were also analyzed under similar conditions, and Fig. 3 shows the results. First, the linear sweep voltammograms (LSV) of the catalysts were measured at a scan rate of 2 mV s<sup>-1</sup>, and the respective polarization curves (Fig. 3g) are plotted after correcting the experimental data with their corresponding ohmic drop (iR-compensation), and then the overpotentials (Fig. 3h) to reach a current density of (10, 50, and 100) mA cm<sup>-2</sup> were calculated. Fig. 3g & h clearly show a volcano-shaped relation for the OER performance of all electrocatalyst, indicating the importance of structural/electronic tuning by the heterojunction of multiple phases. The multi-interfacial dendritic FeCu-BTC/WO<sub>3</sub>-WC hybrid nanocatalyst exhibits excellent OER activity with lowest overpotential of (249, 316, and 340) mV at (10, 50, and 100) mA cm<sup>-2</sup> current density, respectively, compared with the other counterparts; even the overpotential of the benchmark commercial RuO<sub>2</sub> of (326, 393, and 428) mV @ (10, 50, and 100) mA cm<sup>-2</sup>, respectively, is less than that for FeCu-BTC/WO<sub>3</sub>-WC. As can be seen, the OER-active FeCu-MOF when integrated with WO<sub>3</sub> and/or WO<sub>3</sub>-WC outperforms with lower overpotential. The FeCu-BTC/WO<sub>3</sub> delivered (276, 325, and 350) mV overpotential at (10, 50, and 100) mA cm<sup>-2</sup> current density, respectively, and the overpotential of the FeCu-BTC catalyst is (291, 346, and 375) mV at (10, 50, and 100) mA cm<sup>-2</sup> current density, respectively. In addition, the WO<sub>3</sub> exhibits a higher overpotential of (355, 422, and 463) mV at (10, 50, and 100) mA cm<sup>-2</sup> current density, respectively, than that for WO<sub>3</sub>-WC of (313, 365, and 391) mV overpotential at (10, 50, and 100) mA cm<sup>-2</sup> current density, respectively. The bare Ni foam does not show any significant overpotential during OER catalysis. Notably, the redox peaks observed during OER process between 1.28 V and 1.41 V vs RHE (Fig. 3g) is due to their anodic oxidations corresponding to metallic redox couple formation on electrode surface in alkaline medium. These results are associated with the pair of oxidation and reduction (Fe<sup>2+</sup>/Fe<sup>3+</sup>, Cu<sup>+</sup>/Cu<sup>2+</sup>, W<sup>4+</sup>/W<sup>6+</sup>, and Ni<sup>2+</sup>/Ni<sup>3+</sup> redox couple of substrates) peaks before 1.5 V vs RHE and are generally attributed to the reversible electrochemistry of metal hydroxides or oxyhydroxides when the electrodes are swept anodically [39]. The oxidation peak intensity of electrode material in Fig. 3g gradually increases for WO<sub>3</sub> to FeCu-BTC/WO<sub>3</sub>-WC due to the introduction of more metals and the apparent overlapping of redox couples occurs strongly in that potential region [5]. The marked difference in peak potential and the redox peak currents in FeCu-BTC/-WO<sub>3</sub>-WC catalyst depends credibly on the crystalline size, morphological enticement (nanorods to nanodendrite), high surface area of catalyst, and the hybrid spatial arrangements [29]. And, to reduce the pre-OER interferences, reverse OER LSV test of all electrodes were conducted from positive to negative potential regions on RHE scale under similar conditions (Fig. S10, Supporting Information). The OER activity after iR correction (Fig. S10, Supporting Information) showed no obvious changes in the potential and current responses confirming the inherent catalytic property of developed catalysts rather than the intermediate redox couples before the actual OER reaction occurs (Fig. 3g) [45]. The significant OER performance of the FeCu-BTC/-WO<sub>3</sub>-WC is due to the coupling together of two or more functional components in a hybrid dendritic hetero-nanostructure with improved chemical and physical characteristics associated with the synergistic effects that overcome the limitations of the individual components [50]. The Tafel analysis of each electrocatalyst for their OER kinetics was evaluated based on their Tafel slope value obtained after the linear fitting of the overpotential against log( $j$ ) following the Tafel equation in the OER onset regions (Fig. 3i) [11]. The calculated Tafel slope of the FeCu-BTC/WO<sub>3</sub>-WC (22.8 mV dec<sup>-1</sup>), FeCu-BTC/WO<sub>3</sub> (28.2 mV dec<sup>-1</sup>), FeCu-BTC (57.3 mV dec<sup>-1</sup>), WO<sub>3</sub>-WC (65.6 mV dec<sup>-1</sup>), RuO<sub>2</sub> (45.1 mV dec<sup>-1</sup>), and WO<sub>3</sub> (88.7 mV dec<sup>-1</sup>) indicates the favorable OER kinetic mechanisms for all developed electrocatalysts. The lowest Tafel slope for FeCu-BTC/WO<sub>3</sub>-WC manifests a rapid electrochemical

reaction rate that is essentially due to the generation of abundant OER active sites [49]. Furthermore, the AC impedance measurements were carried out for all the electrode materials with a potential referenced at standard current density of  $10 \text{ mA cm}^{-2}$ , and Fig. S11 of the SI depicts the resultant Nyquist plots. The electrochemical impedance spectroscopy (EIS) results further support the rapid electron transfer ability of the dendritic FeCu-BTC/WO<sub>3</sub>-WC nanohybrids with minimum solution resistance ( $R_s$ ) and charge transfer resistance ( $R_{CT}$ ), compared with those of the counterparts, reflecting the lower impedance between the working electrode and the reference electrode, more notably the high conductivity during OER catalysis (Fig. S11, Supporting Information).

Afterward, the accelerated durability test for the OER efficacy of the dendritic FeCu-BTC/WO<sub>3</sub>-WC catalyst was evaluated by the continuous current irradiation of anodic current of (10, 50, and 100)  $\text{mA cm}^{-2}$  by chronopotentiometric (CP) analysis for 30 h and continuous 2000 CV cycle. As shown in Fig. 3j, the FeCu-BTC/WO<sub>3</sub>-WC electrocatalyst showed negligible change in the initial overpotential of only  $\sim 2 \text{ mV}$  at  $j_{10}$ , about  $4 \text{ mV}$  at  $j_{50}$ , and around  $4 \text{ mV}$  at  $j_{100}$ , indicating the supreme catalytic durability for OER applications. The polarization curve plotted for the FeCu-BTC/WO<sub>3</sub>-WC before and after CP analysis (30 h) and 2000 CV cycle assured the excellent OER contender, showing almost cogent curves with negligible shift of the overpotential (Fig. S12a, Supporting Information). Also, the structural persistency of the FeCu-BTC/WO<sub>3</sub>-WC before and after CP analysis (30 h) was checked by the TEM (Fig. S12b, Supporting Information), FE-SEM (Fig. S12c, Supporting Information), and FESEM-EDS elemental color mapping (Fig. S12d1-d5, Supporting Information) which assert the good retention of the original morphology, microstructure, and the elemental distribution, portraying its excellent OER catalysis. All these corroborating outcomes for the robustness of the nanodendritic FeCu-BTC/WO<sub>3</sub>-WC catalyst for OER catalysis may be the result of the fascinating structure, robust electronic correlation of the hybrid nano components, and customary active sites during long-term CP analysis which makes it a

commercially competent OER catalyst (Table S1, Supporting Information).

### 3.3.2. Zinc air battery study

The design of multifunctional and bifunctional electrocatalyst involves the consolidation and assembly of diverse electrocatalytically active centers [6]. Relying on the individual results attained for ORR and OER activity, we explore the bifunctionality based on the potential gaps ( $\Delta E$ ) between the overpotential ( $E_{j_{10}, \text{OER}}$ ) and half-wave potential ( $E_{1/2, \text{ORR}}$ ) of the as-prepared catalyst (Fig. 3k), and more strikingly, the low overvoltage between OER and ORR is recorded for the FeCu-BTC/WO<sub>3</sub>-WC ( $\Delta E = 0.659 \text{ V}$ ) compared with its counterparts, which results in the viability of the catalyst for zinc-air battery application (Fig. 4a, details in supporting information) [43]. The figure-of-merit for the dendritic FeCu-BTC/WO<sub>3</sub>-WC hetero-nanocomposite is then assessed primarily by an open circuit voltage (OCV) test and other electroactivity in a lab-made aqueous Zn-air battery set up in 6 M KOH with 0.2 M zinc acetate electrolyte solution. First, the practical applicability of the dendritic FeCu-BTC/WO<sub>3</sub>-WC and Pt-C + RuO<sub>2</sub> air cathode driven Zn-air battery was tested in the device by measuring the open circuit voltage delivered and is appended as digital photography (Fig. 4b). The potential response for the dendritic FeCu-BTC/WO<sub>3</sub>-WC air cathode apparently conserves the open circuit voltage of  $1.43 \text{ V}$  throughout the time and approaches the closer open circuit voltage of  $1.41 \text{ V}$  for the benchmark Pt-C + RuO<sub>2</sub> air cathode, thus confirming the well-thought-of status of the electrode material for practical Zn-air battery application (Fig. 4c). Furthermore, a well anticipated discharge polarization curve in Fig. 4d indicates that a significantly higher discharge current with perfectly decreased charge-discharge voltage gap for dendritic FeCu-BTC/WO<sub>3</sub>-WC air cathode, compared with that for the commercial benchmark Pt-C + RuO<sub>2</sub> air cathode, demonstrates its high practical rechargeability and the overall air battery performance [50]. The dendritic FeCu-BTC/WO<sub>3</sub>-WC air cathode driven Zn-air

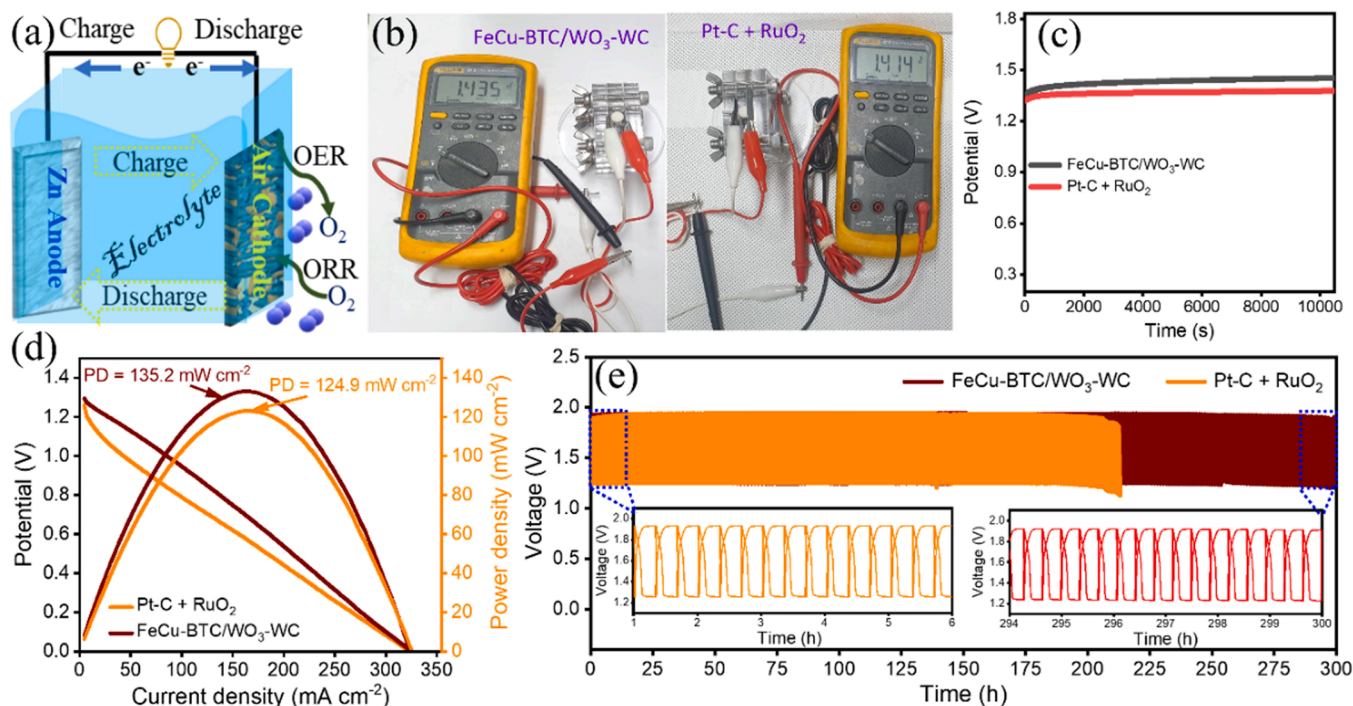


**Fig. 4.** Aqueous zinc-air battery study: (a) Schematic of the lab-made aqueous zinc-air battery based on FeCu-BTC/WO<sub>3</sub>-WC air cathode and zinc foil as air anode. (b) Digital photographs showing the FeCu-BTC/WO<sub>3</sub>-WC and Pt-C + RuO<sub>2</sub> air cathode driven Zn-air battery performance. (c) Open circuit cell voltage of the FeCu-BTC/WO<sub>3</sub>-WC air cathode and commercial benchmark Pt-C + RuO<sub>2</sub> air cathode driven Zn-air battery. (d) The discharge polarization curves and the corresponding power density of the as-synthesized FeCu-BTC/WO<sub>3</sub>-WC and commercial benchmark Pt-C + RuO<sub>2</sub> air cathode driven Zn-air battery. (e) Cycling performance under constant operation of the as-synthesized FeCu-BTC/WO<sub>3</sub>-WC and commercial benchmark Pt-C + RuO<sub>2</sub> air cathode driven Zn-air battery. (Inset: cycling behavior of the FeCu-BTC/WO<sub>3</sub>-WC air cathode driven Zn-air battery for initial and final 6 h operation).

battery outputs a rather high power density of up to  $135.2 \text{ mW cm}^{-2}$  at a current density of  $170 \text{ mA cm}^{-2}$ , outdoing the commercial benchmark Pt-C + RuO<sub>2</sub> air cathode driven Zn-air battery (up to  $124.9 \text{ mW cm}^{-2}$  power density at a current density of  $168 \text{ mA cm}^{-2}$ ) displayed in Fig. 4d, as well as the power density of recently reported bifunctional electrocatalysts (Table S1, Supporting Information).

At the moment, an important parameter of the air battery for its practical applicability was checked by adopting long-term galvanostatic charge–discharge cycling test at  $5 \text{ mA cm}^{-2}$  current density with 0.33 h each of discharge, followed by 0.33 h charge of the dendritic FeCu-BTC/WO<sub>3</sub>-WC air cathode driven Zn-air battery, as well as the commercial benchmark Pt-C + RuO<sub>2</sub> air cathode driven Zn-air battery (Fig. 4e). The charge–discharge average voltage of the dendritic FeCu-BTC/WO<sub>3</sub>-WC air cathode driven Zn-air battery for 300 h reveals only a negligible change in the charge–discharge voltage gap, suggesting the excellent battery durability, but that of the commercial benchmark Pt-C + RuO<sub>2</sub> air cathode driven Zn-air battery for  $\sim 200 \text{ h}$  suffers poor cycling

stability (Fig. 4e). Hence, these sprouting results of the dendritic FeCu-BTC/WO<sub>3</sub>-WC air cathode driven Zn-air battery performance along with outstanding corresponding OER/ORR half-cell reactions support its promising bifunctional oxygen electrocatalysis and prospective use in the metal-air battery as an imminent energy storage device (Table S1, Supporting Information).

### 3.3.3. HER and bifunctional alkaline water electrolysis study

The Pt-like feature of WC in conjunction with the redox capable WO<sub>3</sub> integrated and hybridized high surface area bimetallic-MOF active center convinced us to evaluate the HER activity and the multifunctionality of the FeCu-BTC/WO<sub>3</sub>-WC electrocatalyst. For this, the HER catalysis of all samples was tested in three-electrode set-up in N<sub>2</sub>-saturated 1 M KOH electrolyte. The LSV measurements for the synthesized electrocatalysts and the benchmark commercial Pt-C were conducted at the scan rate of  $2 \text{ mV s}^{-1}$ , and Fig. 5a present the polarization curves after iR compensation. The electrocatalytic HER efficacy based

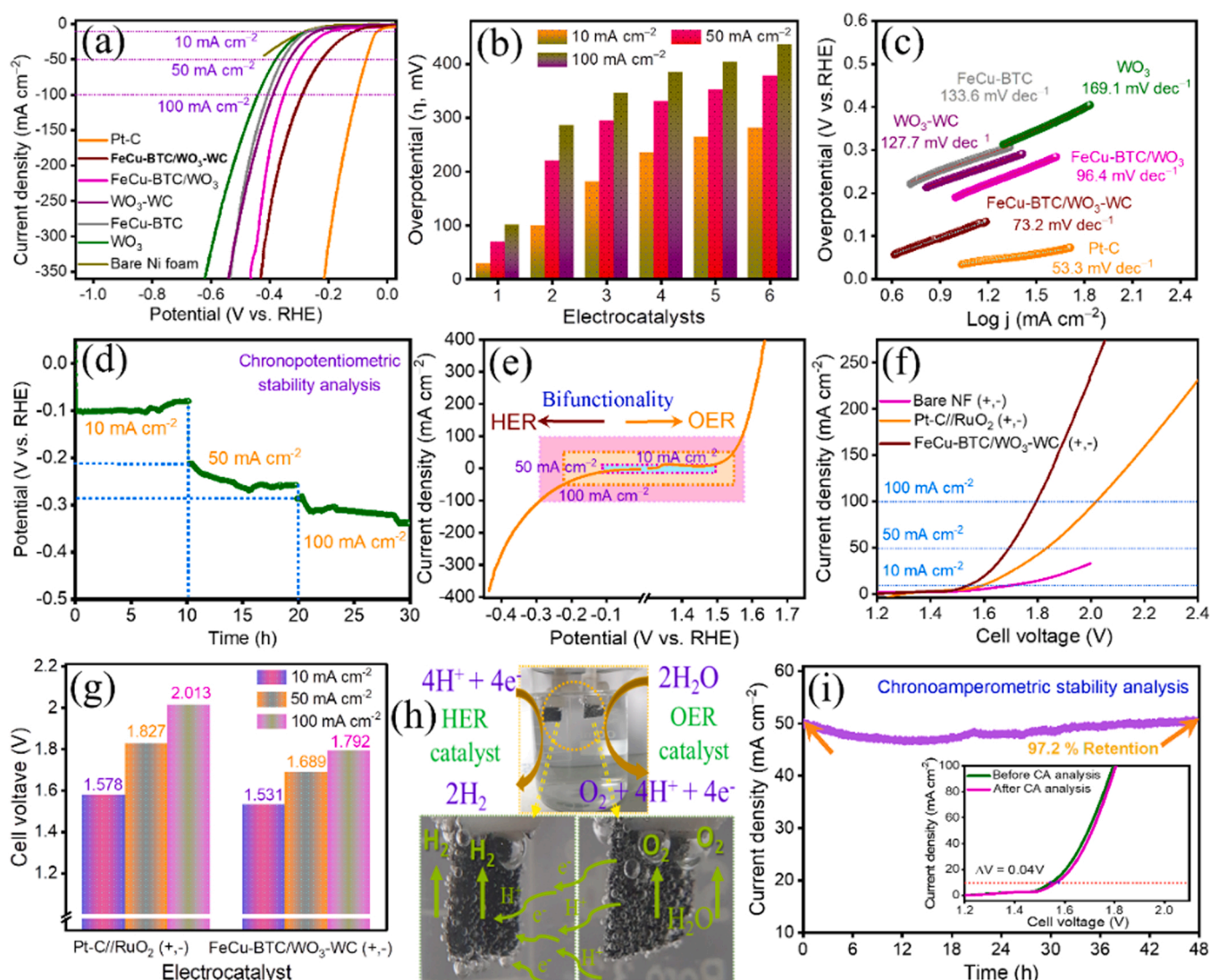


**Fig. 5.** HER and bifunctional overall water electrolysis study: (a–b) LSV polarization curves and the overpotential of (1) Pt-C, (2) FeCu-BTC/WO<sub>3</sub>-WC, (3) FeCu-BTC/WO<sub>3</sub>, (4) WO<sub>3</sub>-WC, (5) FeCu-BTC, and (6) WO<sub>3</sub> for HER. (c) Corresponding Tafel plots and Tafel slope values of electrocatalysts. (d) Chronopotentiometric stability analysis of the dendritic FeCu-BTC/WO<sub>3</sub>-WC at different applied currents. (e) Bifunctionality of the nanodendritic FeCu-BTC/WO<sub>3</sub>-WC via LSV polarization curves of the corresponding HER and OER. (f) LSV polarization curves for two-electrode overall water splitting analysis of the FeCu-BTC/WO<sub>3</sub>-WC (+,–), RuO<sub>2</sub>/Pt-C (+,–), and the bare Ni foam (+,–). (g) Bar diagram showing the comparison of the cell voltage of the RuO<sub>2</sub>/Pt-C (+,–), FeCu-BTC/WO<sub>3</sub>-WC (+,–) at 10, 50, and 100 mA cm<sup>–2</sup>. (h) Digital photograph of the electrode electrolyzer showing the H<sub>2</sub> and O<sub>2</sub> gas evolution during electrochemical water splitting. (i) Chronoamperometric stability analysis of the dendritic FeCu-BTC/WO<sub>3</sub>-WC (+,–) in 1 M KOH solution for 48 h (the inset shows the LSV curves assessed before and after 48 h CA analysis).



on the overpotential to achieve the benchmark current density of (10, 50, and 100) mA cm<sup>-2</sup> is considered. For this, we found that the FeCu-BTC/WO<sub>3</sub>-WC catalyst showed the better catalytic behavior, with lower overpotential of (99, 220, and 286) mV at (10, 50, and 100) mA cm<sup>-2</sup> current density, respectively, showing competitive efficacy with that of the benchmark commercial Pt-C catalyst with overpotential of (29, 69, and 101) mV at (10, 50, and 100) mA cm<sup>-2</sup> current density, respectively (Fig. 5a & b). Other contemporary electrode material also showed considerable HER activity with overpotential ( $\eta$ ) of FeCu-BTC/WO<sub>3</sub> ( $\eta_{10}$  = 181 mV,  $\eta_{50}$  = 294 mV,  $\eta_{100}$  = 346 mV), FeCu-BTC ( $\eta_{10}$  = 265 mV,  $\eta_{50}$  = 352 mV,  $\eta_{100}$  = 404 mV), WO<sub>3</sub>-WC ( $\eta_{10}$  = 236 mV,  $\eta_{50}$  = 330 mV,  $\eta_{100}$  = 385 mV), and WO<sub>3</sub> ( $\eta_{10}$  = 281 mV,  $\eta_{50}$  = 372 mV,  $\eta_{100}$  = 436 mV), as shown in Fig. 5a & b. The well-thought-out material and the multiple heteronanojunction in a single frame of the nanodendritic FeCu-BTC/WO<sub>3</sub>-WC embodies it as the best HER catalyst contender. The electrode kinetics during the HER process for the as-synthesized catalyst was revealed and then presented in their corresponding Tafel plots in Fig. 5c. The Tafel slope calculated for Pt-C, FeCu-BTC/WO<sub>3</sub>-WC, FeCu-BTC/WO<sub>3</sub>, FeCu-BTC, WO<sub>3</sub>-WC, and WO<sub>3</sub> was (53.3, 73.2, 96.4, 133.6, 127.7, and 169.1) mV dec<sup>-1</sup>, respectively. The highly prospective Tafel slope value of the dendritic FeCu-BTC/WO<sub>3</sub>-WC catalyst (Fig. 5c) for HER kinetics ensued as a fine-tuning of the electronic structure during the heterojunction formation, leading to the unique hydrogen transfer pathways provided by the multiple porosity and adsorption of H<sup>+</sup> ion on the catalyst surface. Based on the Tafel slope value, the FeCu-BTC/WO<sub>3</sub>-WC electrocatalyst facilitates the energetically favorable Volmer–Heyrovsky mechanism, leading to the fast release of H<sup>\*</sup> and OH<sup>-</sup> ions on the catalyst surface in the rate-determining step of HER (Volmer mechanism: H<sub>2</sub>O + e<sup>-</sup> → H<sup>\*</sup> + OH<sup>-</sup>; Heyrovsky mechanism: H<sub>2</sub>O + e<sup>-</sup> + H<sup>\*</sup> → H<sub>2</sub> + OH<sup>-</sup>) [4].

The intrinsic catalytic activity and the high electron conductivity of catalysts was then inspected by AC impedance spectroscopy analysis at potential recorded at the benchmark current density of 10 mA cm<sup>-2</sup> to compare the charge transfer resistance of the electrodes. Fig. S13 of the SI clearly implies that the EIS plot of the FeCu-BTC/WO<sub>3</sub>-WC endows a much smaller semicircle in the high-frequency region than its counterparts, proving the accelerated electrode kinetics for HER due to the accessibility of multiple conductive channels with interconnected configurations [18]. The reliable durability and the viability of large-scale industrial H<sub>2</sub> fuel production of the developed nanodendritic FeCu-BTC/WO<sub>3</sub>-WC catalyst was inspected by long-term chronopotentiometric electrochemical stability test at continuous irradiation from lower to higher current density of (10, 50, and 100) mA cm<sup>-2</sup>; Fig. 5d for 10 h each, as well as the consecutive 2000 CV cycles. About (7–9) % overall potential degradation was recorded (Fig. 5d) for over 30 h of analysis, indicating the superior electrode durability and potential of the material for future use. The initial potential degradation is observed when the high current response of 50 mA cm<sup>-2</sup> is applied during CP-HER analysis. The previous study reports a severe stability problem of MOF and the oxide moiety at high cathodic current density possibly due to the growth of adverse catalytically active centers with various microstructural changes such as irregular aggregations, leaching, oxidative decomposition or reconstruction of structure in addition with the possibility of minor peeling out of active catalyst from current collector when swift to large catalytic current densities [43]. The wondering results might be arising due to the activation of some intermediates during cathodic current thus causing in situ oxidation of electrode as discussed in previous reports [15]. But the coherent potential response even after the small loss of initial potential indicates the robustness of the catalyst at high current density of 100 mA cm<sup>-2</sup>. Evidently, the LSV polarization curves with negligible change in overpotential before and after CP and/or 2000 CV cycle plotted in Fig. S14a also is just behind the results obtained for the consistent electrochemical reaction during HER. Furthermore, the morphological changes after 30 h CP analysis were examined by the TEM imagery (Fig. S14b, Supporting Information), FE-SEM imagery (Fig. S14c, Supporting

Information) as well as the FE-SEM-EDS elemental mapping (Fig. S14d–d<sub>5</sub>, Supporting Information). Impressively, the results in Fig. S14 of the SI show no obvious changes in the porous morphology and dendritic shapes, as well as the chemical composition of the FeCu-BTC/WO<sub>3</sub>-WC nanohybrid, indicating the structural toughness, material stability, and practicality for H<sub>2</sub> fuel production. Overall, the HER catalytic competency and the stability of the FeCu-BTC/WO<sub>3</sub>-WC nanohybrid is credited to the inducing of active sites localization on the surface of catalyst, richness in metal oxide–carbide ceramic junctions synergizing with the bimetallic MOF, and the presence of additional H-adsorption sites through the retrieval of metallic centers during the electrochemical process (Table S2, Supporting Information).

Considering the profound performance of the dendritic FeCu-BTC/WO<sub>3</sub>-WC nanocatalyst in the three-electrode cell for HER and OER performance, the bifunctionality of the catalyst (Fig. 5e) was then accessed by coupling the symmetric two-electrode alkaline overall water splitting electrolyzer. The symmetric electrolysis cell with the FeCu-BTC/WO<sub>3</sub>-WC nanodendrite, the commercial Pt-C//RuO<sub>2</sub>, the bare Ni foam, and electrode holder (clamps) as cathode (+) and anode (–) in N<sub>2</sub>-saturated 1 M KOH was then evaluated by the positive scan for LSV within the (1–2.4) V potential range (Fig. 5f & S15). The early onset potential was recorded for the FeCu-BTC/WO<sub>3</sub>-WC (+,–) coupled cell at (1.531, 1.689, and 1.792) V to generate a current of (10, 50, and 100) mA cm<sup>-2</sup>, respectively, and for the benchmark commercial Pt-C//RuO<sub>2</sub> (–,+) at (1.578, 1.827, and 2.013) V to respond to the same current density, respectively (Fig. 5f–g) clearly imitates a proof-of-principle demonstration for green H<sub>2</sub> fuel production. The negligible potential for bare Ni foam (substrate) and electrode holder (clamps) indicates the proficient electrocatalytic role of deposited materials for water splitting reactions. The plethora of H<sub>2</sub> and O<sub>2</sub> gas bubbles emanating from the respective cathode and anode shown in the optical image (Fig. 5h) clearly indicates the bonafide water splitting reaction on the surface of the electrode. Furthermore, the practical aspect of the water electrolyzer was evaluated by a laboratory set-up of an airtight H-cell device to quantify the amount of H<sub>2</sub> and O<sub>2</sub> gas produced with FeCu-BTC/WO<sub>3</sub>-WC (+,–) electrode (Fig. S16, Supporting Information). The volumes of H<sub>2</sub> and O<sub>2</sub> gas were quantified by a water–gas displacement method in separate H-tube and used to calculate the overall Faradaic efficiencies for HER and OER. The theoretical calculated amount of H<sub>2</sub>/O<sub>2</sub> and the measured amount of H<sub>2</sub>/O<sub>2</sub> are plotted and the results show near overlap of these two H<sub>2</sub> releasing processes, rendering a close to 100% Faradaic efficiency for hydrogen production, while the O<sub>2</sub> was released with a Faradaic efficiency of ~94% [4].

In addition to the enhanced electrochemical performances, catalytic durability is an important concern in full-cell water splitting, particularly at high current density or applied potential. For this, the 48 h continuous chronoamperometric (CA) *i*-t stability operation of dendritic FeCu-BTC/WO<sub>3</sub>-WC (+,–) was performed at a constant potential of 1.68 V in 1 M KOH solution in real cell conditions (Fig. 5i). The current response of the FeCu-BTC/WO<sub>3</sub>-WC (+,–) electrolyzer for 48 h did not change substantially (~97.2% retention), indicating the electrochemical stability and robustness of the catalyst for sustainable energy goals. The LSV polarization curve (Fig. 5i, inset) of post-CA analysis also indicates the catalytic efficacy of the FeCu-BTC/WO<sub>3</sub>-WC (+,–) electrolyzer for long-duration usage, showing similar potential response ( $\Delta V$  = 0.04 V) after 48 h. In addition, we performed a *post-operando* analysis of the anode electrode of FeCu-BTC/WO<sub>3</sub>-WC (+,–), following microscopic and composition assessments after electrochemical stability tests to discover the key aspects contributing to the superior catalytic activity and durability. The FE-SEM images (Fig. S17a & b, Supporting Information), TEM image (Fig. S17c, Supporting Information), HRTEM image (Fig. S17d, Supporting Information), HR-TEM image (Fig. S17e, Supporting Information), TEM-EDX elemental mapping images (Fig. S17f & f<sub>1</sub>–f<sub>6</sub>, Supporting Information), and TEM-EDX spectra (Fig. S17f<sub>7</sub>, Supporting Information) of the FeCu-BTC/WO<sub>3</sub>-WC anode electrode after 48 h CA analysis conspicuously preserve the morphology and

crystallinity, as well as the overall elemental composition of the sample. Moreover, the electronic state after continuous 48 h of CA analysis was also inspected by post XPS and Raman study of FeCu-BTC/WO<sub>3</sub>-WC electrode. The chemical state of elements during anodic scan is highly sensitive and hence intensive surface characterization of anode FeCu-BTC/WO<sub>3</sub>-WC electrode was carried out by post-CA XPS analysis. The core level spectra of Fe 2p (Fig. S18a, Supporting Information) at BE 709.1 eV and 712.7 eV (2p<sub>3/2</sub>), 722.2 eV and 723.5 eV (2p<sub>1/2</sub>), 717.2 eV and 735.8 eV (satellite peak) genuinely indicate the presence of Fe<sup>+2</sup>/Fe<sup>+3</sup> ion of iron. The high intense Fe<sup>+3</sup> peaks signify the abundant stable metal oxyhydroxide intermediate species in catalyst, likely to be the real active center for the OER, which can improve the charge transfer kinetics thereby increasing the water oxidation activity [39]. The HR-XPS spectrum of Cu 2p centered at 932.7 eV and 934 eV (2p<sub>3/2</sub>), 952.6 eV and 954.7 eV (2p<sub>1/2</sub>), 942.1 eV and 962.4 eV (satellite peak) signal the stable state of Cu in bimetallic BTC MOF structure. Obviously, the intense Cu<sup>+</sup> peaks and satellite peaks indicate the reduction of Cu<sup>++</sup> species markedly showing an important role during the electrochemical OER process (Fig. S18b, Supporting Information) [30]. Moreover, the duplet spectrum centered at 32.6 eV and 34.7 eV signify W<sup>+4</sup> 4f<sub>7/2</sub> while the more intense peaks at 34.9 eV and 36.9 eV attributed to the high valence W<sup>+6</sup> 4f<sub>5/2</sub>, possibly due to surface oxidation of W during anodic scan for 48 h (Fig. S18c, Supporting Information). Evidently, the non-metallic counterparts C 1s (Fig. S18d, Supporting Information) and O 1s (Fig. S18e, Supporting Information) of FeCu-BTC/WO<sub>3</sub>-WC catalyst do not reflect any surface reconstruction property except an additional O-H bond at 535 eV in O 1s spectra, generally assigned as trapped hydrogen ions in catalyst during OER stability test. Also, Fig. S19, Supporting Information depicts the surface valence state of the respective elements in FeCu-BTC/WO<sub>3</sub>-WC cathode electrode after 48 h of CA analysis. The Fe 2p metal peaks after HER (Fig. S19a, Supporting Information) doesn't show remarkable change except some BE shift (~0.4 eV) with prominent satellite shake up peaks, indicating the formation of Fe ions with lower oxidation state than normal due to charge imbalance in neighboring sites [29]. The Cu 2p spectrum in Fig. S19b, Supporting Information showed the high intense Cu<sup>+</sup> ions than the Cu<sup>+2</sup> ions due to charge transfer during electrochemical reaction. The deconvoluted W 4f (Fig. S19c, Supporting Information) spectra possesses a stable surface electronic state during HER reaction. The prolonged electronic state of C 1s and O 1s in oxide-carbide and MOF after CA stability test was affirmed from deconvoluted C 1s spectra (Fig. S19d, Supporting Information) and O 1s spectra (Fig. S19e, Supporting Information) with a broadened O-H bond in O 1s spectra, possibly due to residual hydrogen ions trapped into the catalyst. Furthermore, as an ideal indication of catalytic stability, the dissolution of catalytic elements (electrocatalytic leaching) in electrolyte was analyzed by inductively coupled plasma-optical emission spectrometry (ICP-OES). The results quantified after 48 h high potential CA stability analysis showed the small leaching off Cu (~0.02 ppm) accompanied by no detectable Fe or W elements in the solution. The results after stability analysis revealed that there is negligible dissolution of catalyst material in alkaline electrolyte and no negative effect of leaching of Cu, indeed the dissolution of Cu in solution possibly open up the structure leading to the maximum contact area of electrolytes and density of catalytic surface sites [51]. The chemical bonding and structure of the FeCu-BTC/-WO<sub>3</sub>-WC catalyst before and after 48 h CA analysis were further investigated by Raman spectra (Fig. S20, Supporting Information). The Raman modes observed at 131.6, 180.2, 268.4 cm<sup>-1</sup> (WO<sub>3</sub> bending modes), 719.5, 811.1 cm<sup>-1</sup> (stretching modes) of bridging oxides are consistent after the long-term CA stability test. The sharp peaks at 330.2, 1555.3 and 811.1 cm<sup>-1</sup> represent the co-existence of WO<sub>3</sub> and WC in the composite catalysts suggesting a robust structure after electrocatalytic stability test [15]. The Raman spectrum centered at 1610 cm<sup>-1</sup> (benzene ring stretch mode), 1555.3 cm<sup>-1</sup> (carboxylate group) corresponding to BTC MOF broadened after long term CA test (Fig. S20, Supporting Information), an indication of electronic modulation as consistent with the

post-XPS study (Fig. S18-19, Supporting Information) and previous reports [29]. Also, the absence of Raman bands in the 500 – 700 cm<sup>-1</sup> indicates the absence of tungstate ion in the catalyst after 48 h CA stability analysis, consistent with the results obtained from the ICP-OES results (not obvious W ion in the electrolyte). In principle, the specific interfacial interactions of WO<sub>3</sub>-WC boast a longer lifetime of charge carrier than WO<sub>3</sub> where the WC interface modulates the electron density around WO<sub>3</sub> (SMO) optimizing the chemisorption of water splitting intermediates leading to high chemical and structural durability. The electrochemical stability of WO<sub>3</sub> and composite catalyst is preferably due to the formation of a stable WO<sub>3</sub>-WC interface which is not exactly on the surface, mostly confined with the FeCu-BTC MOF thus, having less chance of direct contact with the electrolyte and WO<sub>3</sub>-WC hence, prevent its dissolution in electrolyte and formation of K<sub>2</sub>WO<sub>4</sub> at the same time. Overall, the integration of the multiple phases and the composition makes the electrode very stable even under high potential condition for longer time period, upholding the morphological structure and the elemental dispensation. The persistent electrocatalytic property and stability of FeCu-BTC/WO<sub>3</sub>-WC nanodendrite catalyst arises as a result of the junction interface between organic-inorganic hybrid components resulting  $\pi$ -d electronic coupling of ligand to metal site, efficient organic-inorganic dual active sites exposure, improved electrical conductivity with enormous oxalate ions, and developed polarizability on catalysts surface [52]. From all the excellent electrochemical results acquired for the dendritic FeCu-BTC/WO<sub>3</sub>-WC nanostructure along with the structural and compositional consistency is primarily due to the presence of polyvalence tungsten oxide-carbide heterojunction and highly interconnected bimetallic MOF integrity. Thus, the dendritic FeCu-BTC/WO<sub>3</sub>-WC nanocomposite brings up the promising practical application of the water electrolysis and green hydrogen fuel production, as compared to the counterpart electrocatalysts (Table S2, Supporting Information).

To better understand the charge transfer mechanism, electronic behaviour, enhanced catalytic activity, and the affinity for FeCu-BTC/WO<sub>3</sub>-WC intermediates, the densities of state (DOS) were assessed from density functional theory (DFT) calculation based on the interaction of H atoms on the optimal site. Fig. 6a-e represents the DFT optimization chemical models of individual catalysts and the interface models bridging based on the lattice-matching planes [11,53]. The DOS of WO<sub>3</sub>, WO<sub>3</sub>-WC (inorganic) and FeCu-BTC (organics) shown in Fig. 6f possesses obvious density of states at Fermi level, itself signaling a good conductivity of organic and inorganic individuals. The coupling of organics with inorganics (FeCu-BTC/WO<sub>3</sub>; Fig. 6f) results in improved density of state distribution at Fermi level portraying enhanced conductivity due to presence of dual organic-inorganic active sites [52]. The band structure of FeCu-BTC/WO<sub>3</sub>-WC (Fig. 6f) clearly illustrates the dominance of electronic states close to the Fermi level, superior to other counterparts, suggesting a greater binding possibility, quick electron transfer, and higher catalytic activity [54]. The higher fermi level of FeCu-BTC/WO<sub>3</sub>-WC catalyst with broadened peaks can be attributed to the orbital hybridization implying enhanced electron donation capability and catalyst surface activation. Moreover the significant band structure in lower energy level corresponding to s-p hybridized bonding orbitals and the p-d components of the active centers in higher energy level of FeCu-BTC/WO<sub>3</sub>-WC catalyst actually represents the fundamental insight of organic-inorganic hybrid interfaces (Fig. 6f) [23]. Hence, a multimodal FeCu-BTC/WO<sub>3</sub>-WC nanodendritic electrocatalyst achieve ultrafast electrocatalytic performance due to generation of multiple heterochannels between catalyst-catalyst and catalyst-electrolyte. Based on the intriguing electrocatalytic results and the previously reported findings, the drawbacks of one catalyst compensate the others, leading to the mutual synergism between multiple crystalline phases of FeCu-BTC/WO<sub>3</sub>-WC nanodendritic electrocatalyst with strong metal support interaction (SMSI) principle. Based on Sobatier's principle, the atomic hydrogen adsorption free energy ( $\Delta G_H$ ) on W site of WO<sub>3</sub> is high, and the presence of few active sites hinders the

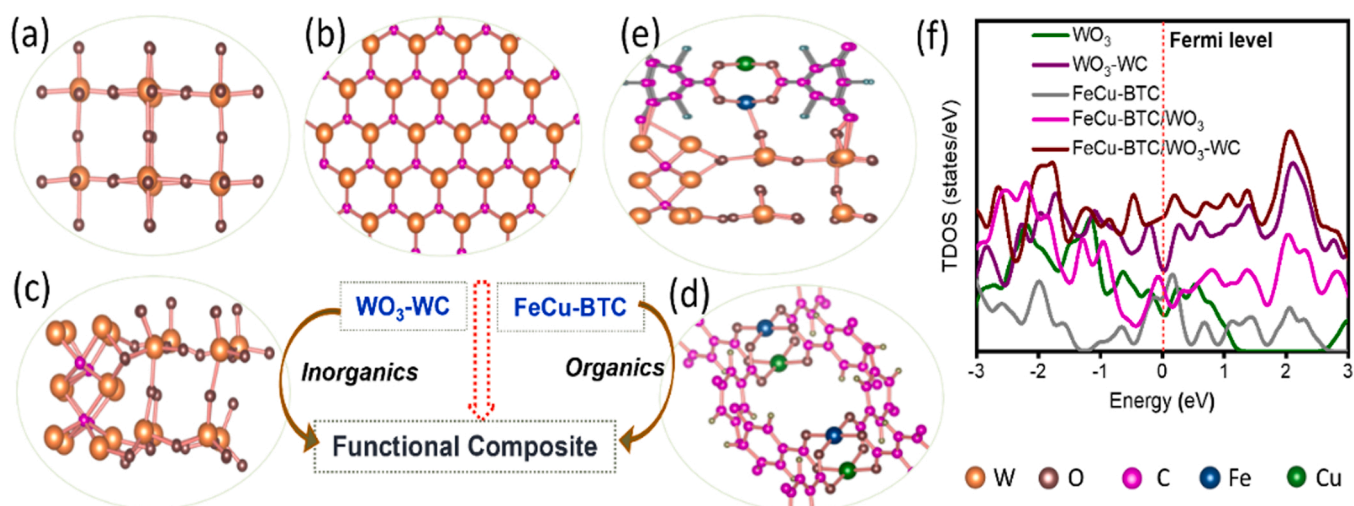


**Fig. 6.** DFT optimization chemical models of (a)  $\text{WO}_3$ , (b) WC, (c)  $\text{WO}_3\text{-WC}$ , (d) FeCu-BTC, (e) FeCu-BTC/ $\text{WO}_3\text{-WC}$ . (f) total density of states (TDOS) of electrocatalysts.

electrochemical HER, but an effective strategy aiming at the modulation of the electronic structure by coupling with its carbide counterparts boosts the ORR and HER activity together [55]. Indeed, the exposed W atoms in the top layer of WC surfaces facilitate  $\text{O}^*$ ,  $\text{OH}^*$  adsorption at HER and ORR potentials, and the hexagonal  $\text{WO}_3$  interfaces act as the real active sites for  $\text{H}^+$  adsorption, forming an electron reservoir that promotes catalytic properties [56]. Yet another, the strong metal d-orbitals and O-p orbitals of BTC overlap and hybridize together, resulting in metal-oxygen ligation (each metal coordinatively ligated with four carboxylic O atoms), thus leading to the adequate stability of the FeCu-BTC MOF. The Cu element promotes the reduction of  $\text{Fe}^{+3}$  and its polyvalent state, because the d-band center of Fe near the Fermi level is induced to accept the electrons, increase the kinetics of O-O bond cleavage, and accelerate the electron transfer between different elements. With the increased electron density around Fe atoms, the electron transfer to adsorb oxygen catalysis species is improved, the oxygen exchange rate is accelerated, and are the real active sites of the electrocatalytic OER and ORR processes [40]. Overall, the active species in the enhanced electrocatalytic performance of FeCu-BTC/ $\text{WO}_3\text{-WC}$  are the plentiful redox coupling between Fe-Cu, as well as the redox interaction of  $\text{WO}_3\text{-WC}$  with multiple heterojunctions and best organic-inorganic synergetic influence.

#### 4. Conclusion

In this work, a unique pseudomorphic transformation synthesis protocol to fabricate highly crystalline  $\text{WO}_3\text{-WC}$  nanorods was adopted to achieve the utmost morphological retention by a typical hydrothermal reaction, followed by a reduction/carbonization process, and then integrated with the FeCu-BTC MOF moiety for the first time to procure the multifunctionality in electrocatalyst (FeCu-BTC/ $\text{WO}_3\text{-WC}$ ). The featured nanodendritic morphology with plentiful nanopores, dense oxide-carbide/MOF heterointerfaces, and high interface polarization leading electronic modulation established FeCu-BTC/ $\text{WO}_3\text{-WC}$  as a potential electrocatalyst. Meanwhile, the ceramic  $\text{WO}_3\text{-WC}$  nanorods stitched with the FeCu-BTC MOF exhibits promising electrocatalytic performance in half-cell reactions (HER, OER, ORR) and the full cell device (water splitting and zinc-air battery), with high chance of admirable electrocatalyst alternative. Conclusively, our novel approach of coupling the multiple interfaces along with the choice of multi-component elemental composition and two or more functional components in nanodendritic structure might be the future material in the direction of green hydrogen production, energy storage, and environment remediation goal.

#### CRediT authorship contribution statement

**Dasu Ram Paudel:** Conceptualization, Methodology, Investigation, Validation, Formal analysis, Writing – original draft. **Uday Narayan Pan:** Methodology, Data curation, Formal analysis, Visualization, Writing – review & editing. **Ram Babu Ghising:** Methodology, Data curation, Visualization. **Mani Ram Kandel:** Methodology, Data curation, Visualization. **Sampath Prabhakaran:** DFT calculation. **Do Hwan Kim:** DFT calculation. **Nam Hoon Kim:** Conceptualization, Writing – review & editing, supervision. **Joong Hee Lee:** Conceptualization, Writing – review & editing, Supervision, Project administration.

#### Declaration of Competing Interest

The authors declare that they have no known competing financial interest or personal relationship that could have appeared to influence the work reported in this paper.

#### Data availability

Data will be made available on request.

#### Acknowledgements

This work was supported by the Basic Science Research Program (2022R1A2C2010339) and the Regional Leading Research Center Program (2019R1A5A8080326) through the National Research Foundation funded by the Ministry of Science and ICT of the Republic of Korea.

#### Appendix A. Supporting information

Supplementary data associated with this article can be found in the online version at doi:10.1016/j.apcatb.2023.122711.

#### References

- [1] R. Hanna, D.G. Victor, Marking the decarbonization revolutions, *Nat. Energy* 6 (2021) 568–571, <https://doi.org/10.1038/s41560-021-00854-1>.
- [2] Z.Y. Yu, Y. Duan, X.Y. Feng, X. Yu, M.R. Gao, S.H. Yu, Clean and affordable hydrogen fuel from alkaline water splitting: past, recent progress, and future prospects, *Adv. Mater.* 33 (2021) 1–35, <https://doi.org/10.1002/adma.202007100>.
- [3] M. Chatenet, B.G. Pollet, D.R. Dekel, F. Dionigi, J. Deseure, P. Millet, R.D. Braatz, M.Z. Bazant, M. Eikerling, I. Staffell, P. Balcombe, Y. Shao-Horn, H. Schäfer, Water electrolysis: from textbook knowledge to the latest scientific strategies and



- industrial developments, *Chem. Soc. Rev.* 51 (2022) 4583–4762, <https://doi.org/10.1039/d0cs01079k>.
- [4] T.I. Singh, A. Maibam, D.C. Cha, S. Yoo, R. Babarao, S.U. Lee, S. Lee, High-alkaline water-splitting activity of mesoporous 3D heterostructures: an amorphous-shell/crystalline-core nano-assembly of Co-Ni-phosphate ultrathin-nanosheets and V-doped cobalt-nitride nanowires, *Adv. Sci.* (2022) 2201311, <https://doi.org/10.1002/advs.202201311>.
  - [5] U.N. Pan, D.R. Paudel, A. Kumar Das, T.I. Singh, N.H. Kim, J.H. Lee, Ni-nanoclusters hybridized 1T-Mn-VTe<sub>2</sub> mesoporous nanosheets for ultra-low potential water splitting, *Appl. Catal. B Environ.* 301 (2022), 120780, <https://doi.org/10.1016/j.apcatb.2021.120780>.
  - [6] Y. Zhang, Y. Lin, T. Duan, L. Song, Interfacial engineering of heterogeneous catalysts for electrocatalysis, *Mater. Today* 48 (2021) 115–134, <https://doi.org/10.1016/j.mattod.2021.02.004>.
  - [7] C.C. Gudal, U.N. Pan, D.R. Paudel, M.R. Kandel, N.H. Kim, J.H. Lee, Bifunctional P-Intercalated and Doped Metallic (1T)-Copper Molybdenum Sulfide Ultrathin 2D-Nanosheets with Enlarged Interlayers for Efficient Overall Water Splitting, *ACS Appl. Mater. Interfaces* 14 (2022) 14492–14503, <https://doi.org/10.1021/acsmi.2c00278>.
  - [8] Y.Z. Wang, M. Yang, Y.M. Ding, N.W. Li, L. Yu, Recent advances in complex hollow electrocatalysts for water splitting, *Adv. Funct. Mater.* 32 (2022) 1–19, <https://doi.org/10.1002/adfm.202108681>.
  - [9] D.R. Paudel, U.N. Pan, T.I. Singh, C.C. Gudal, N.H. Kim, J.H. Lee, Fe and P Doped 1T-Phase Enriched WS<sub>2</sub> 3D-Dendritic Nanostructures for Efficient Overall Water Splitting, *Appl. Catal. B Environ.* 286 (2021), 119897, <https://doi.org/10.1016/j.apcatb.2021.119897>.
  - [10] M. Singh, T.T. Nguyen, P. Muthu Austeria, Q.P. Ngo, D.H. Kim, N.H. Kim, J.H. Lee, J. Metallic metastable hybrid 1T'/1T phase triggered Co,P SnS<sub>2</sub> nanosheets for high efficiency trifunctional electrocatalyst, *Small* (2023), <https://doi.org/10.1002/smll.202206726>.
  - [11] F. Hu, D. Yu, M. Ye, H. Wang, Y. Hao, L. Wang, L. Li, X. Han, S. Peng, Lattice-matching formed mesoporous transition metal oxide heterostructures advance water splitting by active Fe–O–Cu bridges, *Adv. Energy Mater.* 12 (2022) 2200067, <https://doi.org/10.1002/aenm.202200067>.
  - [12] Y.H. Li, P.F. Liu, L.F. Pan, H.F. Wang, Z.Z. Yang, L.R. Zheng, P. Hu, H.J. Zhao, L. Gu, H.G. Yang, Local atomic structure modulations activate metal oxide as electrocatalyst for hydrogen evolution in acidic water, *Nat. Commun.* 6 (2015), <https://doi.org/10.1038/ncomms9064>.
  - [13] T. Zheng, W. Sang, Z. He, Q. Wei, B. Chen, H. Li, C. Cao, R. Huang, X. Yan, B. Pan, S. Zhou, J. Zeng, Conductive tungsten oxide nanosheets for highly efficient hydrogen evolution, *Nano Lett.* 17 (2017) 7968–7973, <https://doi.org/10.1021/acs.nanolett.7b04430>.
  - [14] H. Sun, X. Xu, Y. Song, W. Zhou, Z. Shao, Designing high-valence metal sites for electrochemical water splitting, *Adv. Funct. Mater.* 31 (2021), <https://doi.org/10.1002/adfm.202009779>.
  - [15] R. Rajalakshmi, A. Rebekah, C. Viswanathan, N. Ponpandian, Evolution of intrinsic 1-3D WO<sub>3</sub> nanostructures: tailoring their phase structure and morphology for robust hydrogen evolution reaction, *Chem. Eng. J.* 428 (2022), 132013, <https://doi.org/10.1016/j.cej.2021.132013>.
  - [16] D.R. Paudel, U.N. Pan, R.B. Ghising, P.P. Dhakal, V.A. Dinh, H. Wang, N.H. Kim, J. H. Lee, Interface modulation induced by the 1T Co-WS<sub>2</sub> shell nanosheet layer at the metallic NiTe<sub>2</sub>/Ni core-nanoskeleton: Glib electrode-kinetics for HER, OER, and ORR, *Nano Energy* 102 (2022), 107712, <https://doi.org/10.1016/j.nanoen.2022.107712>.
  - [17] S. Adhikari, M. Murmu, D. Kim, Core-shell engineered WO<sub>3</sub> architectures: recent advances from design to applications, *Small* 18 (2022) 2202654, <https://doi.org/10.1002/smll.202202654>.
  - [18] F. Wang, B. Dong, J. Wang, N. Ke, C. Tan, A. Huang, Y. Wu, L. Hao, L. Yin, X. Xu, Y. Xian, S. Agathopoulos, Self-supported porous heterostructure WC/WO<sub>3-x</sub> ceramic electrode for hydrogen evolution reaction in acidic and alkaline media, *J. Adv. Ceram.* 11 (2022) 1208–1221, <https://doi.org/10.1007/s40145-022-0604-4>.
  - [19] Y. Yang, X. Shao, S. Zhou, P. Yan, T.T. Isimjan, X. Yang, Interfacial electronic coupling of NC@WO<sub>3</sub>-W<sub>2</sub>C decorated Ru clusters as a reversible catalyst toward electrocatalytic hydrogen oxidation and evolution reactions, *ChemSusChem* 14 (2021) 2992–3000, <https://doi.org/10.1002/cssc.202100893>.
  - [20] T. Van Nguyen, H.H. Do, M. Tekalgne, Q. Van Le, T.P. Nguyen, S.H. Hong, J. H. Cho, D. Van Dao, S.H. Ahn, S.Y. Kim, WS<sub>2</sub>-WC-WO<sub>3</sub> nano-hollow spheres as an efficient and durable catalyst for hydrogen evolution reaction, *Nano Conver.* 8 (2021), <https://doi.org/10.1186/s40580-021-00278-3>.
  - [21] C. Xie, W. Chen, S. Du, D. Yan, Y. Zhang, J. Chen, B. Liu, S. Wang, In-situ phase transition of WO<sub>3</sub> boosting electron and hydrogen transfer for enhancing hydrogen evolution on Pt, *Nano Energy* 71 (2020), 104653, <https://doi.org/10.1016/j.nanoen.2020.104653>.
  - [22] A. Salah, L. Zhang, H. Tan, F. Yu, Z. Lang, N. Al-Ansi, Y. Li, Advanced Ru/Ni/WC@NPC multi-interfacial electrocatalyst for efficient sustainable hydrogen and chlor-alkali Co-production, *Adv. Energy Mater.* 12 (2022) 2200332, <https://doi.org/10.1002/aenm.202200332>.
  - [23] S.C. Sun, H. Jiang, Z.Y. Chen, Q. Chen, M.Y. Ma, L. Zhen, B. Song, C.Y. Xu, Bifunctional WC-supported RuO<sub>2</sub> nanoparticles for robust water splitting in acidic media, *Angew. Chem. - Int. Ed.* 61 (2022), <https://doi.org/10.1002/anie.202202519>.
  - [24] Z. Li, M. Hu, P. Wang, J. Liu, J. Yao, C. Li, Heterojunction catalyst in electrocatalytic water splitting, in: *Coord. Chem. Rev.* 439, 2021, 213953, <https://doi.org/10.1016/j.ccr.2021.213953>.
  - [25] R.B. Ghising, U.N. Pan, D.R. Paudel, M.R. Kandel, N.H. Kim, J.H. Lee, A hybrid trimetallic-organic framework-derived N, C co-doped Ni-Fe-Mn-P ultrathin nanosheet electrocatalyst for proficient overall water-splitting, *J. Mater. Chem. A* (2022), <https://doi.org/10.1039/D2TA02470E>.
  - [26] M. Babu, A. Rhan, S. Ramakrishnan, N. Logeshwaran, S. Kumar, H. Joo, D. Jin, Integrating the essence of metal organic framework-derived ZnCoTe-N-C/MoS<sub>2</sub> cathode and ZnCo-NPS-N-CNT as anode for high-energy density hybrid supercapacitors, *Compos. Part B* 247 (2022), 110339, <https://doi.org/10.1016/j.compositesb.2022.110339>.
  - [27] Y. Wang, L. Zhao, J. Ma, J. Zhang, Confined interface transformation of metal organic frameworks for highly efficient oxygen evolution reaction, *Energy Environ. Sci.* (2022), <https://doi.org/10.1039/d2ee01073a>.
  - [28] M. Kato, N. Fujibayashi, D. Abe, N. Matsubara, S. Yasuda, I. Yagi, Impact of heterometallic cooperativity of iron and copper active sites on electrocatalytic oxygen reduction kinetics, *ACS Catal.* 11 (2021) 2356–2365, <https://doi.org/10.1021/acscatal.0c04753>.
  - [29] Z. Li, S. Deng, H. Yu, Z. Yin, S. Qi, L. Yang, J. Lv, Z. Sun, M. Zhang, Fe-Co-Ni trimetallic organic framework chrysanthemum-like nanoflowers: efficient and durable oxygen evolution electrocatalysts, *J. Mater. Chem. A* 10 (2022) 4230–4241, <https://doi.org/10.1039/D1TA09658C>.
  - [30] S. Naik Shreyanka, J. Theerthagiri, S.J. Lee, Y. Yu, M.Y. Choi, Multiscale design of 3D metal-organic frameworks (M-BTC, M: Cu, Co, Ni) via PLAL enabling bifunctional electrocatalysts for robust overall water splitting, *Chem. Eng. J.* 446 (2022), 137045, <https://doi.org/10.1016/j.cej.2022.137045>.
  - [31] Y. Yan, L. Zhang, X. Qi, H. Song, J.Y. Wang, H. Zhang, X. Wang, Template-free pseudomorphic synthesis of tungsten carbide nanorods, *Small* 8 (2012) 3350–3356, <https://doi.org/10.1002/smll.201200877>.
  - [32] J.C. Lytle, N.R. Denny, R.T. Turgeon, A. Stein, Pseudomorphic transformation of inverse opal tungsten oxide to Tungsten carbide, *Adv. Mater.* 19 (2007) 3682–3686, <https://doi.org/10.1002/adma.200700717>.
  - [33] M.R. Kandel, U.N. Pan, D.R. Paudel, P.P. Dhakal, N.H. Kim, J.H. Lee, Hybridized bimetallic phosphides of Ni-Mo, Co-Mo, and Co-Ni in a single ultrathin-3D-nanosheets for efficient HER and OER in alkaline media, *Compos. Part B Eng.* 239 (2022), 109992, <https://doi.org/10.1016/j.compositesb.2022.109992>.
  - [34] X. Jiang, H. Jang, S. Liu, Z. Li, M.G. Kim, C. Li, Q. Qin, X. Liu, J. Cho, The Heterostructure of Ru<sub>2</sub>P/WO<sub>3</sub>/NPC Synergistically Promotes H<sub>2</sub>O Dissociation for Improved Hydrogen Evolution, *Angew. Chem.* 133 (2021) 4156–4162, <https://doi.org/10.1002/ange.202014411>.
  - [35] K. Cho, S.-H. Han, M.P. Suh, Copper-organic framework fabricated with CuS nanoparticles: synthesis, electrical conductivity, and electrocatalytic activities for oxygen reduction reaction, *Angew. Chem. Int. Ed.* 55 (2016) 15301–15305, <https://doi.org/10.1002/anie.201607271>.
  - [36] Z. Zhang, P. Chen, X. Duan, K. Zang, J. Luo, X. Duan, Robust epitaxial growth of two-dimensional heterostructures, multiheterostructures, and superlattices, *Science* 357 (80) (2017) 788–792, <https://doi.org/10.1126/science.aan6814>.
  - [37] T. Rodenas, I. Luz, G. Prieto, B. Seoane, H. Miro, A. Corma, F. Kapteijn, F. X. Llabrés, I. Xamena, J. Gascon, Metal-organic framework nanosheets in polymer composite materials for gas separation, *Nat. Mater.* 14 (2015) 48–55, <https://doi.org/10.1038/nmat4113>.
  - [38] L. Tian, X. Yu, J. Xu, R. Wang, Z. Xu, T. Chen, Preparation and study of tungsten carbide catalyst synergistically codoped with Fe and nitrogen for oxygen reduction reaction, *J. Mater. Res. Technol.* 15 (2021) 7100–7110, <https://doi.org/10.1016/j.jmrt.2021.11.134>.
  - [39] L. Ding, K. Li, Z. Xie, G. Yang, S. Yu, W. Wang, H. Yu, J. Baxter, H.M. Meyer, D. A. Cullen, F.Y. Zhang, Constructing ultrathin W-doped NiFe nanosheets via facile electrosynthesis as bifunctional electrocatalysts for efficient water splitting, *ACS Appl. Mater. Interfaces* 13 (2021) 20070–20080, <https://doi.org/10.1021/acsmi.1c01815>.
  - [40] H. Li, H. Shi, Y. Dai, H. You, S. Raj Babu Arulmani, H. Zhang, C. Feng, L. Huang, T. Zeng, J. Yan, X. Liu, A co-doped oxygen reduction catalyst with FeCu promotes the stability of microbial fuel cells, *J. Colloid Interface Sci.* 628 (2022) 652–662, <https://doi.org/10.1016/j.jcis.2022.07.068>.
  - [41] P.C. Lohani, A.P. Tiwari, K. Chhetri, A. Muthurasu, B. Dahal, S.-H. Chae, T.H. Ko, J. Y. Lee, Y.S. Chung, H.Y. Kim, Polypyrrole nanotunnels with luminal and abluminal layered double hydroxide nanosheets grown on a carbon cloth for energy storage applications, *ACS Appl. Mater. Interfaces* 14 (2022) 23285–23296, <https://doi.org/10.1021/acsmi.1c24585>.
  - [42] T. Mukhiya, B. Dahal, G.P. Ojha, K. Chhetri, M. Lee, T. Kim, S.-H. Chae, A. P. Tiwari, A. Muthurasu, H.Y. Kim, Silver nanoparticles entrapped cobalt oxide nanohairs/electrospun carbon nanofibers nanocomposite in apt architecture for high performance supercapacitors, *Compos. Part B Eng.* 178 (2019), 107482, <https://doi.org/10.1016/j.compositesb.2019.107482>.
  - [43] J. Diao, Y. Qiu, S. Liu, W. Wang, K. Chen, H. Li, W. Yuan, Y. Qu, X. Guo, Interfacial engineering of W<sub>2</sub>N/WC heterostructures derived from solid-state synthesis: a highly efficient trifunctional electrocatalyst for ORR, OER, and HER, *Adv. Mater.* 1905679 (2020) 1–11, <https://doi.org/10.1002/adma.201905679>.
  - [44] Y.Y. Ma, Z.L. Lang, L.K. Yan, Y.H. Wang, H.Q. Tan, K. Feng, Y.J. Xia, J. Zhong, Y. Liu, Z.H. Kang, Y.G. Li, Highly efficient hydrogen evolution triggered by a multi-interfacial Ni/WC hybrid electrocatalyst, *Energy Environ. Sci.* 11 (2018) 2114–2123, <https://doi.org/10.1039/c8ee01129j>.
  - [45] W. Li, C. Li, H. Dong, X. Zhang, J. Liu, M. Song, G. Wang, L. Zhao, H. Sheng, B. Chen, H. Zhang, Expediting oxygen evolution by optimizing cation and anion complexity in electrocatalysts based on metal phosphorous trichalcogenides, *Angew. Chem. - Int. Ed.* 570228 (2022), <https://doi.org/10.1002/ange.202214570>.
  - [46] L. Casillas-Trujillo, B. Osinger, R. Lindblad, D. Karlsson, A.I. Abrikosov, S. Fritze, K. Von Fieandt, B. Alling, I. Hotz, U. Jansson, I.A. Abrikosov, E. Lewin,

- Experimental and theoretical evidence of charge transfer in multi-component alloys-how chemical interactions reduce atomic size mismatch, *Mater. Chem. Front.* 5 (2021) 5746–5759, <https://doi.org/10.1039/d1qm00380a>.
- [47] P.P. Dhakal, U.N. Pan, D.R. Paudel, M.R. Kandel, N.H. Kim, J.H. Lee, Cobalt-manganese sulfide hybridized Fe-doped 1T-vanadium disulfide 3D-hierarchical core-shell nanorods for extreme low potential overall water-splitting, *Mater. Today Nano* 20 (2022), 100272, <https://doi.org/10.1016/j.mtnano.2022.100272>.
- [48] M. Singh, T.T. Nguyen, J. Balamurugan, N.H. Kim, J.H. Lee, Rational manipulation of 3D hierarchical oxygenated nickel tungsten selenide nanosheet as the efficient bifunctional electrocatalyst for overall water splitting, *Chem. Eng. J.* 430 (2022), 132888, <https://doi.org/10.1016/j.cej.2021.132888>.
- [49] K. Chang, D.T. Tran, J. Wang, S. Prabhakaran, D.H. Kim, N.H. Kim, J.H. Lee, Atomic heterointerface engineering of Ni<sub>2</sub>P-NiSe<sub>2</sub> nanosheets coupled ZnP-based arrays for high-efficiency solar-assisted water splitting, *Adv. Funct. Mater.* (2022), <https://doi.org/10.1002/adfm.202113224>.
- [50] J. Diao, Y. Qiu, S. Liu, W. Wang, K. Chen, H. Li, W. Yuan, Y. Qu, X. Guo, Interfacial engineering of W<sub>2</sub>N/WC heterostructures derived from solid-state synthesis: a highly efficient trifunctional electrocatalyst for ORR, OER, and HER, *Adv. Mater.* 32 (2020) 1905679, <https://doi.org/10.1002/adma.201905679>.
- [51] X. Chen, Z. Qiu, H. Xing, S. Fei, J. Li, L. Ma, Y. Li, D. Liu, Sulfur-doping/leaching induced structural transformation toward boosting electrocatalytic water splitting, *Appl. Catal. B Environ.* 305 (2022), 121030, <https://doi.org/10.1016/j.apcatb.2021.121030>.
- [52] O.T. Hofmann, E. Zojer, L. Hörmann, A. Jeindl, R.J. Maurer, First-principles calculations of hybrid inorganic-organic interfaces: from state-of-the-art to best practice, *Phys. Chem. Chem. Phys.* 23 (2021) 8132–8180, <https://doi.org/10.1039/d0cp06605b>.
- [53] Y.-L.T. Ngo, K.C. Bhamu, A. Voronova, J. Jana, S.G. Kang, J.S. Chung, W.M. Choi, J.H. Jang, S.H. Hur, B. Seo, Carbide-directed enhancement of electrochemical hydrogen evolution reaction on tungsten carbide-oxide heterostructure, *Chem. Eng. J.* 450 (2022), 137915, <https://doi.org/10.1016/j.cej.2022.137915>.
- [54] H. Wang, X. Zhang, F. Yin, W. Chu, B. Chen, Coordinately unsaturated metal-organic framework as an unpyrolyzed bifunctional electrocatalyst for oxygen reduction and evolution reactions, *J. Mater. Chem. A* 8 (2020) 22111–22123, <https://doi.org/10.1039/d0ta04331a>.
- [55] G.-Q. Yu, B.-Y. Huang, S.-M. Chen, J.-W. Liao, W.-J. Yin, G. Teobaldi, X.-B. Li, The combined role of faceting and heteroatom doping for hydrogen evolution on a WC electrocatalyst in aqueous solution: a density functional theory study, *J. Phys. Chem. C* 125 (2021) 4602–4613, <https://doi.org/10.1021/acs.jpcc.0c11104>.
- [56] G. Mineo, M. Scuderi, E. Bruno, S. Mirabella, Engineering hexagonal/monoclinic WO<sub>3</sub> phase junctions for improved electrochemical hydrogen evolution reaction, *ACS Appl. Energy Mater.* 5 (2022) 9702–9710, <https://doi.org/10.1021/acsaem.2c01383>.